Icarus 206 (2010) 390–409

Contents lists available at ScienceDirect

Icarus

journal homepage: www.elsevier.com/locate/icarus

N-body simulations of viscous instability of planetary rings

Heikki Salo [a,*], Jürgen Schmidt [b]

[a] Dept. of Physical Sciences, Astronomy Division, Univ. of Oulu, P.O. Box 3000, FIN-90014 Oulun yliopisto, Finland
[b] Universität Potsdam, Karl-Liebknecht-Str. 24/25, D-14476 Potsdam-Golm, Germany

ARTICLE INFO

Article history:
Received 5 January 2009
Revised 16 June 2009
Accepted 19 July 2009
Available online 4 August 2009

Keywords:
Collisional physics
Planetary rings
Saturn, Rings

ABSTRACT

We study viscous instability of planetary rings in terms of N-body simulations. We show that for rings composed of fairly elastic particles (e.g. as in Hatzes et al. [Hatzes, A., Bridges, F.G., Lin, D.N.C., 1988. Collisional properties of ice spheres at low impact velocities. Mon. Not. R. Astron. Soc. 231, 1091–1115]) the instability may lead to the spontaneous formation of dense ringlets in a background of lower density. In most parts of Saturn's rings the particle collisions are probably much more dissipative, as suggested by the presence of self-gravity wakes, and classic viscous instability should be suppressed. However, our results demonstrate that the mechanism of viscous instability itself is valid. The dynamical effects of size-dependent elasticity in a system with a size distribution have never been studied before. We show that this may in principle lead to a size-selective viscous instability, small particles concentrating on ringlets against the more uniform background of large particles.

1. Introduction

The viscous instability (or diffusion instability; Lukkari, 1981; Ward, 1981; Lin and Bodenheimer, 1981) was one of the prime explanations proposed for the radial density variations of Saturn's B ring discovered in Voyager fly-bys. This mechanism is based on the assumption that there is a large collision-induced difference between the kinetic temperatures of rarefied (dynamically hot) and dense (cool) portions of the rings. In this case the dynamic viscosity (product of shear viscosity and density) may decrease with optical depth, leading to a collisional flux of particles which is directed toward local density maxima, i.e. to an amplification of density variations.

Nevertheless, the viscous instability was later discarded, mainly because theoretical (Araki and Tremaine, 1986; Araki, 1991) and simulation studies (Wisdom and Tremaine, 1988) indicated that viscous instability is not obtained, at least not when a constant coefficient of restitution, or velocity-dependent elasticity laws resembling those found in the laboratory experiments of frost-covered ice particles (Bridges et al., 1984) are assumed. Such elasticity models imply a highly flattened steady-state for all optical depths, and the lack of instability was attributed to the dominant role of nonlocal viscosity, which leads to dynamic viscosity increasing monotonically with optical depth; this nonlocal contribution was neglected in the earlier studies where ad-hoc viscosity versus density laws had been assumed.

Our purpose here, over two decades later, is to remind that the viscous instability mechanism itself is valid, and should at least be kept in mind when explanations for various ring structures are sought for. Whether or not the condition for instability is fulfilled depends largely on the still poorly-known elasticity of ring particles. For example, elasticity formulae resembling those found in the experiments of particles with compacted frost in their surfaces (Hatzes et al., 1988) imply a rather hot low optical depth steady-state dominated with strong local viscosity. In the case of identical particles this leads to a viscosity–density relation which indeed fulfills the instability condition for optical depths around unity (Salo, 1991; Latter and Ogilvie, 2008). Moreover, allowing for particle size distribution, range of elastic properties, and perhaps for additional physical factors like particle adhesion, may further promote viscous instabilities. In this paper, we provide the first direct demonstration of viscous instability in terms of 3D N-body simulations using the Hatzes et al. formula, and compare it with linear isothermal stability analysis. The simulation results confirm the predicted stability boundary and the asymptotic long-wavelength growth rates, though the minimum unstable wavelength is nearly 10 times larger than the predicted one. The non-uniform quasi-steady bimodal state – the co-existence of dynamically cool dense ringlets and hot rarefied zones – reached after the saturation of simulated instability is also analyzed in detail.

The plan of the paper is as follows: In Section 2 we briefly review the hydrodynamical treatment of dense planetary rings and the isothermal linear stability condition. In Section 3 we use small-scale local simulations to evaluate the pressure and viscosity versus density relations entering the analysis. The two above

* Corresponding author.
E-mail address: heikki.salo@oulu.fi (H. Salo).

0019-1035/$ - see front matter © 2009 Elsevier Inc. All rights reserved.
doi:10.1016/j.icarus.2009.07.038

mentioned elasticity laws (Bridges et al., 1984; Hatzes et al., 1988) are compared, representing prototypes of very inelastic and elastic cases; for simplicity we concentrate on the case of identical, non-gravitating particles. In Section 4 larger scale simulations are performed, both with and without self-gravity: we check the linear growth rates implied by hydrodynamical analysis, and follow the nonlinear saturation; we also demonstrate that the dense portions of the bimodal state may exhibit self-gravity wake structures. In Section 5, we discuss other examples of viscous instability, including Lukkari (1981) indirect simulations, as well as 2D simulations; the 2D simulations are illuminating as they allow to follow the longer time scale evolution of the bimodal state. In Section 6 we discuss the relevance of simulations to the structure in Saturn's rings, and speculate about other variants of viscous instability; we also show preliminary simulation examples of selective instabilities in systems with a range of particle sizes and elastic properties. Conclusions are given in Section 7.

2. Theoretical background: linear isothermal dispersion relations

The local steady-state properties of dense planetary rings, including vertical thickness, velocity dispersion, and viscosity, are governed by the energy balance between the viscous gain of energy from the differential rotation associated with the orbital motion ($\dot{E}_{gain}$) and the energy dissipated in inelastic impacts between ring particles ($\dot{E}_{diss}$). The time-scale for achieving this energy balance is short, a few tens of impacts per particle at most, which is on the order of an orbital period for dense rings. On much longer time-scales, the ring evolution is determined by the radial flow of angular momentum: the stability properties of this flow depend sensitively on the elastic properties of particles via the implied local energy balance. The crucial factor is the dependence of steady-state viscosity on density.

To illustrate how the properties of the radial flow differ for different viscosity versus density relations, we review briefly the isothermal linear stability analysis of dense rings (see Schmit and Tscharnuter, 1995; Schmidt et al., 2001). Restricting to the axisymmetric case, the vertically integrated hydrodynamic balance equations for continuity and momentum read (see e.g. Shu and Stewart, 1985; Stewart et al., 1984)

$$\frac{\partial\sigma}{\partial t}+\frac{1}{r}\frac{\partial(r\sigma u_r)}{\partial r}=0, \tag{1}$$

$$\sigma\left(\frac{\partial}{\partial t}+u_r\frac{\partial}{\partial r}\right)u_r=\sigma\frac{u_\theta^2}{r}-\sigma\frac{\partial(\Phi_{cen}+\Phi_{sg})}{\partial r}-\frac{1}{r}\frac{\partial(rP_{rr})}{\partial r}, \tag{2}$$

$$\sigma\left(\frac{\partial}{\partial t}+u_r\frac{\partial}{\partial r}+\frac{u_r}{r}\right)u_\theta=-\frac{1}{r^2}\frac{\partial(r^2P_{r\theta})}{\partial r}, \tag{3}$$

where σ denotes the surface density, u_r and u_θ are the radial and tangential mean velocities, P_{rr} and $P_{r\theta}$ are components of the pressure tensor $\widehat{\mathbf{P}}$, and the gravitational potential contains contributions from the central field Φ_{cen} and the axisymmetric ring self-gravity Φ_{sg}. These equations follow from the zeroth and first order velocity moments of the Boltzmann equation for the particle distribution function; the second order moment equations would describe the evolution of the pressure tensor components (Stewart et al., 1984). In the hydrodynamic fluid approximation the equations for the four independent pressure tensor components are replaced by a single energy equation, describing how the kinetic temperature (velocity dispersion) establishes as a balance of viscous energy gain, collisional dissipation, and heat transfer. Since our interest here is on viscous *instability* which evolves in time-scales much longer than the orbital period, we neglect the energy equation and assume that the energy balance $\dot{E}_{gain}=\dot{E}_{diss}$ is instantaneously achieved.[1] Moreover, instead of solving analytically for the energy balance, we will use pressure tensor components directly determined from particle simulations in Section 3, after a steady-state has been achieved.

Denoting with $u\equiv u_r$ and $v\equiv u_\theta-v_{orb}$ the mean velocities in the frame rotating with the orbital velocity v_{orb} at the distance r, taking into account that $v_{orb}^2=r\partial\Phi_{cen}/\partial r$, and ignoring terms $\propto u^2,\ v^2,\ uv$, as well as curvature terms, these equations simplify to

$$\frac{\partial\sigma}{\partial t}=-\frac{\partial(\sigma u)}{\partial r}, \tag{4}$$

$$\frac{\partial u}{\partial t}=2\Omega v-\frac{1}{\sigma}\frac{\partial P_{rr}}{\partial r}-\frac{\partial\Phi_{sg}}{\partial r}, \tag{5}$$

$$\frac{\partial v}{\partial t}=-\frac{1}{2}\Omega u-\frac{1}{\sigma}\frac{\partial P_{r\theta}}{\partial r}. \tag{6}$$

To proceed further we assume that the pressure tensor has the standard Newtonian form which describes how the kinetic pressure reacts on compression and shear. This implies

$$\begin{aligned}P_{rr}&=p-\left(\frac{4}{3}+\frac{\zeta}{\nu}\right)\nu\sigma\frac{\partial u}{\partial r},\\ P_{r\theta}&=-(\sigma\nu)\left(s+\frac{\partial v}{\partial r}\right),\end{aligned} \tag{7}$$

where $p=\frac{1}{3}tr\widehat{\mathbf{P}}$ is the isotropic vertically integrated pressure, ν and ζ are the kinematic shear and bulk viscosity, and $s=-\frac{3}{2}\Omega$ denotes the systematic shear rate. In the isothermal analysis, omitting the energy equation, it assumed that p and ν depend solely on σ; in particular the parametrization $\nu\propto\sigma^\beta$ will be adopted.

These equations allow a steady-state solution where the surface density has a constant value σ_0, and velocity deviations vanish, $u_0=v_0=0$. For constant density the self-gravitational force is also zero. Denoting small perturbations from this ground state with subscript '1', we have $\sigma=\sigma_0+\sigma_1,\ u=u_1,\ v=v_1,\ \Phi_{sg}=\Phi_1$. Inserting these into the hydrodynamic equations, and keeping only linear terms, yields

$$\frac{\partial\sigma_1}{\partial t}=-\sigma_0\frac{\partial u_1}{\partial r}, \tag{8}$$

$$\frac{\partial u_1}{\partial t}=2\Omega v_1-\frac{\partial\Phi_1}{\partial r}-\frac{1}{\sigma_0}\left.\frac{\partial p}{\partial\sigma}\right|_{\sigma=\sigma_0}\frac{\partial\sigma_1}{\partial r}+\left(\zeta_0+\frac{4}{3}\nu_0\right)\frac{\partial^2u_1}{\partial r^2}, \tag{9}$$

$$\frac{\partial v_1}{\partial t}=-\frac{1}{2}\Omega u_1-\frac{3\Omega}{2\sigma_0}\left.\frac{\partial(\nu\sigma)}{\partial\sigma}\right|_{\sigma=\sigma_0}\frac{\partial\sigma_1}{\partial r}+\nu_0\frac{\partial^2v_1}{\partial r^2}. \tag{10}$$

Furthermore, the perturbations in gravity and surface density are connected through the Poisson equation

$$\frac{\partial^2\Phi_1}{\partial r^2}+\frac{\partial^2\Phi_1}{\partial z^2}=4\pi G\sigma_1\delta(z). \tag{11}$$

We assume that the perturbations have the form of an infinite axisymmetric plane wave, $\sigma_1,u_1,v_1\propto\exp(\omega t+ikr)$. In this case the Poisson equation has a solution

$$\Phi_1(r,z)=-\frac{2\pi G}{|k|}\sigma_1\exp(-|kz|), \tag{12}$$

and the potential perturbation can be eliminated in terms of the density perturbation

$$\left.\frac{\partial\Phi_1}{\partial r}\right|_{z=0}=-\frac{2\pi G}{|k|}\frac{\partial\sigma_1}{\partial r}. \tag{13}$$

[1] On the other hand, as shown by Schmidt et al. (2001; see also Spahn et al., 2000), inclusion of energy equation is important for the hydrodynamical analysis of *overstable* oscillations having time-scales comparable to the orbital period.

The requirement of non-trivial solutions to Eqs. (8-10) leads to the third-order dispersion relation (Schmit and Tscharnuter, 1995; hereafter ST1995),

$$\omega^3+\omega^2k^2\left(\zeta_0+\frac{7}{3}\nu_0\right)+\omega\left[\Omega^2-2\pi G\sigma_0|k|+c_0^2k^2+\left(\zeta_0+\frac{4}{3}\nu_0\right)\nu_0k^4\right]+\left[2\pi G\sigma_0|k|+c_0^2k^2+3\Omega^2(1+\beta)\right]\nu_0k^2=0, \quad (14)$$

which connects the perturbation wavelength $\lambda=\frac{2\pi}{k}$ to its complex frequency ω. The positive real part $Re(\omega)$ implies a growing unstable solution, while a non-zero imaginary part implies an oscillating component. Here, $\beta\equiv\partial\log\nu/\partial\log\sigma$, and $c_0^2\equiv\partial p/\partial\sigma$, both evaluated at the ground-state. As discussed in ST1995, in general one of the roots of the dispersion relation is real, while the other two roots form a complex conjugate pair. The conjugate pair, if the real part is positive, corresponds to viscous overstability, while the real root, again if positive, corresponds to viscous instability.

ST1995 illustrated that for 'typical' values of B-ring viscosity and pressure (they adopted $\nu_0=54\,\mathrm{cm^2/s}$ and $c_0=0.2\,\mathrm{cm/s}$, and assumed $\zeta_0/\nu_0=1$), the system should be overstable for perturbations with wavelengths exceeding about 100 m, provided that $\beta>\beta_{cr}$. At the long wavelength limit $\beta_{cr}=(\zeta_0/\nu_0-2/3)/3$ (= 1/9 for $\nu_0=\zeta_0$) if self-gravity is omitted, whereas with inclusion of gravity β_{cr} shifts to slightly negative values. However, numerical simulations (Salo et al., 2001) indicated that the actual condition of overstability is much more stringent, with $\beta_{cr}\sim1$. To account for this discrepancy, Spahn et al. (2000) and Schmidt et al. (2001) suggested that the isothermal stability analysis had to be augmented by the inclusion of the energy equation, leading to a fourth order dispersion relation, where the coefficients include additional terms like derivatives of viscosity, pressure, and energy dissipation and gain with respect to kinetic temperature, and the transport coefficient for the kinetic heat transfer. Indeed, the agreement to simulations was markedly improved when non-isothermal treatment was performed, using transport coefficient and temperature derivatives based on simulation measurements in Salo et al. (2001). Besides the additional temperature terms, the extra stabilization was attributed partly to $\zeta_0/\nu_0>1$ found in the simulation measurements. However, it is hard to interpret the physical origin of the implied bulk viscosity, and it seems now that its appearance was an artifact related to using the hydrodynamic approximation in a situation where it is not really applicable: for example, the assumed Newtonian pressure tensor does not take into account the changes in the shape of the velocity ellipsoid. In this sense the recent kinetic theory analysis of Latter and Ogilvie (2006, 2008), including a full set of seven moment equations, is a more appropriate description, moreover leading to much improved agreement with simulations.

Concerning viscous instability, the isothermal dispersion relation predicts that in the non-gravitating case the condition $\beta<-1$ should lead to instability (ST1995; see also Ward, 1981; Lin and Bodenheimer, 1981). In terms of dynamic viscosity $\eta=\nu\tau\propto\sigma^{\beta+1}$, this condition is equivalent to $\frac{\partial\eta}{\partial\tau}<0$. The condition $\beta<-1$ can also be seen directly from linearized perturbation equations. Ignoring the Laplacian term in Eq. (10) for the tangential momentum implies $u_1\approx-3(1+\beta)\frac{\nu_0}{\sigma_0}\frac{\partial\sigma_1}{\partial r}$, and inserting this in the continuity Eq. (8) yields a radial diffusion equation

$$\frac{\partial\sigma_1}{\partial t}\approx3(1+\beta)\nu_0\frac{\partial^2\sigma_1}{\partial r^2}. \quad (15)$$

If $1+\beta$ is negative this indicates negative diffusion, i.e. flux toward density maxima. The growth rate is

$$Re(\omega)=-3\nu_0k^2(1+\beta), \quad (16)$$

which also follows from the full set of linearized equations on the long wavelength limit. With the inclusion of axisymmetric self-gravity, the linear stability condition for instability is slightly shifted (ST1995) to $\beta<-1+1/(3Q^2)$, where $Q=c\Omega/(\pi G\sigma_0)$ is the Toomre parameter (Toomre, 1964). Contrary to the overstability, the conditions for viscous instability should not be greatly affected if the hydrodynamic analysis is replaced by the more accurate kinetic theory stability analysis (Latter and Ogilvie, 2008). Note also that bulk viscosity does not affect the predicted stability boundary, nor the asymptotic long wavelength growth rate.

While the stability/instability boundary is set by β (and Q if axisymmetric gravity is included), the length and time scales of instability depend also on ν_0 and c_0^2: for a fixed β the minimum unstable wavelength scales roughly as c_0/Ω, while the expected fastest growth rate scales roughly proportional to $\nu_0(c_0/\Omega)^{-2}$.

3. Measurement of the viscosity versus density relation

In order to evaluate the viscosity over density relation for a given particle elasticity law we turn to local simulations. An advantage of a local method is that the surface density of the system can be fixed, controlled via the number of particles N and the size of the calculation region A_0. Provided that the scale of the system is small compared to the wavelength of any unstable perturbation (overstability or instability) the system remains, after an initial transient evolution, in the ground state. We can directly tabulate the ground state pressure and viscosity as a function of density, by time averaging over all particle orbits and impacts, once the energy balance has been established. The obtained values of ν, p, β can then be used to predict the linear stability properties against infinitesimal perturbations.

3.1. Local simulation method

The calculations are restricted to a local comoving cell, with dimension much smaller than the orbital radius. Linearized dynamical equations are employed, and the particles leaving the simulation system are subject to periodic boundary conditions (Wisdom and Tremaine, 1988, see also Toomre and Kalnajs, 1991). The particle motion is governed by

$$\begin{aligned}\ddot{x}-2\Omega\dot{y}+(\Omega_r^2-4\Omega^2)x&=F_x,\\ \ddot{y}+2\Omega\dot{x}&=F_y,\\ \ddot{z}+\Omega_z^2z&=F_z,\end{aligned} \quad (17)$$

where the x-axis points in the radial direction, the y-axis in the direction of orbital motion, and the z-axis is perpendicular to the equatorial plane. The reference point of the coordinate system moves with angular velocity Ω in a circular orbit at a radial distance a. In the case of a central point mass, considered in this paper, the epicyclic frequency Ω_r and the frequency Ω_z of vertical oscillations are both identical to Ω. The right hand side consists of additional forces, e.g. due to impacts or self-gravity. In the absence of external forces the solution of these equations describes epicycles: at the distance x the guiding centers drift with the mean velocity $(\Omega_r^2-4\Omega^2)/(2\Omega)x$, which reduces to $-\frac{3}{2}\Omega x$ for a central point mass.

Two different methods are employed for the calculation of impacts: we either treat impacts as instantaneous velocity changes, or include the impact forces between any (slightly) overlapping particle pair (see Salo, 1995 for detailed description of the impact calculations). As shown in Salo (1995) both methods yield similar results, the force method however being a more natural choice in the case of strongly gravitating particles, in particular when gravity leads to the formation of semi-permanent aggregates (Salo, 1995; Karjalainen and Salo, 2004; Morishima and Salo, 2006). In this section we concentrate on non-gravitating simulations, for which we use the somewhat faster instantaneous impact method.

3.2. Tabulation of pressure tensor components

By definition, the components of the pressure tensor $P_{\alpha\beta}$ give the amount of the β-component of momentum transferred in the α-direction, per unit area and unit time. The flow of momentum consists of the *local* contribution, related to the momentum carried radially by the particles' random motions, and the *nonlocal* contribution, resulting from the momentum transferred from one particle to another during a collision. When evaluating the momentum flow in simulations, it is convenient to include all particles and impacts, regardless of their vertical coordinate. This corresponds to the vertical averaging assumed in the hydrodynamic treatment of Section 2.

Let $c_i = \{\dot{x}_i, \dot{y}_i, \dot{z}_i\} - \{0, -3/2\Omega x_i, 0\}$ denote the random velocity of particle i. The local contribution to $\widehat{\mathbf{P}}$ is obtained by adding the momentum mc_β carried by each of the N particles, moving with velocity component c_α with respect to the mean flow, leading to

$$P^{local}_{\alpha\beta} = \frac{1}{A_0}\sum_i^N (c_\alpha)_i (mc_\beta)_i = \sigma\overline{c_\alpha c_\beta}, \tag{18}$$

where A_0 denotes the area of the simulation region and the bar indicates averaging over particles. Once the steady-state has been achieved, one can improve the accuracy by averaging over time, $\langle P^{local}_{\alpha\beta}\rangle$. The standard formula for nonlocal momentum transfer is (Wisdom and Tremaine, 1988)

$$P^{nonlocal}_{\alpha\beta} = \frac{1}{A_0\Delta t}\sum_{impacts} \Delta r_\alpha m_>(\delta c_\beta)_>, \tag{19}$$

where the summation is over all impacts occurring during the time interval Δt, and $m_>(\delta c_\beta)_>$ denotes the change of the momentum in the β direction of the particle with the larger r_α coordinate, and Δr_α the absolute difference in the r_α-coordinates of the impacting particles.

In the hydrodynamical treatment the P_{xy} component measured at the steady state (with $v_0 = 0$) is identified with $-s\sigma\nu$ (see Eq. (7); we will from here on replace the subscripts r, θ by x, y, respectively, to be consistent with the nomenclature used in local simulations). In the case of Keplerian shear, $s = -\frac{3}{2}\Omega$, and assuming identical particles the above equations give

$$\nu_{local} = \frac{2}{3\Omega}\langle\overline{c_x c_y}\rangle, \tag{20}$$

$$\nu_{nonlocal} = \frac{2}{3\Omega}\frac{1}{N\Delta t}\sum_{impacts}\Delta x(\delta c_y)_>. \tag{21}$$

In the non-gravitating case studied here we will systematically replace σ by geometric optical depth τ. The kinematic shear viscosities are not affected by this; the dynamic viscosity will from here on be identified with $\eta = \tau\nu$. In the hydrodynamic analysis the partial derivative of viscosity with respect to density is needed: we will identify this with the difference of the ground-state viscosities at different optical depths.

In a similar manner as viscosities, the local and nonlocal pressures are identified with

$$p_{local} = \frac{1}{3}\left(P^{local}_{xx} + P^{local}_{yy} + P^{local}_{zz}\right) = \frac{1}{3}\tau\langle\overline{c_x^2 + c_y^2 + c_z^2}\rangle \equiv \tau c^2,$$

$$p_{nonlocal} = \frac{1}{3}\left(P^{nonlocal}_{xx} + P^{nonlocal}_{yy} + P^{nonlocal}_{zz}\right),$$

$$= \frac{1}{3}\frac{1}{N\Delta t}\sum_{impacts}\left[\Delta x(\delta c_x)_> + \Delta y(\delta c_y)_> + \Delta z(\delta c_z)_>\right]. \tag{22}$$

Here, c stands for the one-dimensional velocity dispersion. Following ST1995 we will write the total pressure in the form $p = c_0^2\tau$, with the assumption that the effective (i.e. including effects of nonlocal pressure) velocity dispersion c_0 is fixed. The partial derivative $\frac{\partial p}{\partial\tau}$ is thus replaced by p/τ.

3.3. Viscosity versus density relations for systems of frosty and smooth ice particles

We have made systematic measurements of ground-state properties versus optical depth, for two different elasticity models which describe the laboratory measurements of ice particles with different surface properties (Fig. 1). The Bridges et al. (1984) formula,

$$\varepsilon_n(v_n) = \max\left[(v_n/v_c)^{-0.24}, 0.25\right]\ (v_n > v_c) = 1\ (v_n \leqslant v_c), \tag{23}$$

with $v_c \equiv v_B = 0.0077$ cm/s, describes the elasticity of frost covered ice at temperature of 124 K; ε_n is the normal coefficient of restitution, and v_n is the normal component of the impact velocity. This formula has been widely used in previous studies, including the pioneering simulations by Wisdom and Tremaine (1988). The steady-state properties following from this elasticity law were reported in detail in Salo et al. (2001). The other elasticity model, studied in detail here, is based on Hatzes et al. (1988) measurements for particles with compacted frost at their surfaces (20 cm particles at temperature of 123 K)

$$\varepsilon_n(v) = 0.90e^{-0.22v_n} + 0.01\,v_n^{-0.6}, \tag{24}$$

where v_n is expressed in units of cm/s (see Eq. (1) in Hatzes et al., 1988). Compared to Bridges et al. "frosty particle" formula, this "smooth particle" model implies a much shallower drop of elasticity with impact velocity. Note that Hatzes et al. (1988) report experiments with even more elastic particles: their "polished" ice measurements, with very smooth particle surfaces, indicate $\varepsilon_n \geqslant 0.8$ for the whole range $v_n \leqslant 2$ cm/s displayed in Fig. 1.

The importance of the adopted elasticity model on the dynamics of a planetary ring stems from the fact that it determines the collisional energy balance. The rate of energy dissipated in impacts (per unit mass) can be written as

$$\dot{E}_{diss} = k_1\omega_c c^2(1 - \varepsilon_n^2), \tag{25}$$

where ω_c is the impact frequency, and k_1 (like k_2 and k_3 below) is a numerical coefficient of order unity; in the case of velocity-depen-

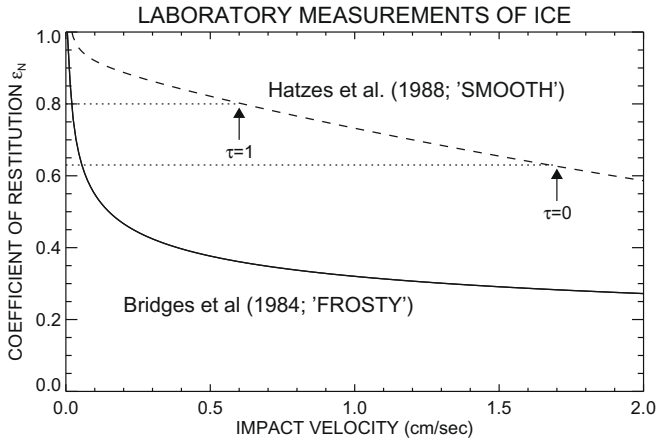

Fig. 1. Elastic models applied in simulations, leading to qualitatively different stability properties. The solid line denotes a fit to laboratory measurements with frosty ice particles Bridges et al., 1984, whereas the dashed line corresponds to measurements where particles had compacted surfaces Hatzes et al., 1988, leading to considerably less dissipative impacts. Note that actual measurements had a large scatter around these fitted functions. The horizontal dotted lines indicate the theoretical ε_{cr} values (see Fig. 2) for $\tau = 0$ and 1, while arrows indicate the corresponding impact velocity for the Hatzes et al. elasticity formula; the actual average impact velocities in simulations are slightly smaller, $\sqrt{\langle v_n^2\rangle} = 1.2$ and 0.43 cm/s for $\tau = 0$ and 1, respectively.

dent elasticity ε_n can be defined as an effective mean value averaged over impacts. The viscous gain is given by

$$\dot{E}_{gain} = s^2 \nu = \frac{9}{4}\Omega^2 \nu, \tag{26}$$

where ν contains the local and nonlocal components. The basic expression for local viscosity is $\nu_{local} = \omega_c l^2$, where l is the radial mean free path. In the high impact frequency regime the impacts limit the mean free path to $\propto c/\omega_c$ while for low ω_c an upper bound is set by the amplitude of epicyclic excursions, $l \propto c/\Omega$. Combining these estimates, and approximating $\omega_c \sim \tau\Omega$, leads to the Goldreich and Tremaine (1978) interpolation formula

$$\nu_{local} = k_2 \frac{c^2}{\Omega} \frac{\tau}{1+\tau^2}. \tag{27}$$

For the nonlocal component, dimensional arguments (Shukhman, 1984) suggest that

$$\nu_{nonlocal} \propto \omega_c R^2 = k_3 \Omega R^2 \tau, \tag{28}$$

where R is the particle radius. The energy balance $\dot{E}_{diss} = \dot{E}_{gain}$ thus implies

$$k_1 \Omega \tau c^2 (1-\varepsilon_n^2) = \frac{9}{4}\Omega^2 \left(k_2 \frac{c^2}{\Omega} \frac{\tau}{1+\tau^2} + k_3 \Omega R^2 \tau \right). \tag{29}$$

For a given elasticity law, Eq. (29) determines the average elasticity and velocity dispersion, and thereby also viscosity, as a function of optical depth.

Which of the two viscous gain contributions dominate in Eq. (29) depends on the kinetic temperature of the system. In the case of a hot system, $c/(R\Omega) \gg 1$, the local contribution dominates in the limit $\tau \to 0$. If the nonlocal gain term is ignored, the c^2 dependence of Eq. (29) cancels out: the energy balance requires that the effective value of ε_n attains a critical value ε_{cr}, which depends on the optical depth via the relation

$$(1-\varepsilon_{cr}^2)(1+\tau^2) = \frac{9k_2}{4k_1} \approx 0.61 \tag{30}$$

(Goldreich and Tremaine, 1978; numerical factor from Stewart et al., 1984). The corresponding steady-state velocity dispersion c_{st} is then determined by the $\varepsilon_n(v_n)$ relation. When $d\varepsilon_n/dv_n < 0$, like indicated by the above mentioned laboratory measurements, the steady-state is thermally stable: for example, $c > c_{st}$ implies on the average faster, more dissipative impacts leading to the cooling of the system. Likewise, if $c < c_{st}$ the impacts are too elastic to balance the energy gain, leading to heating of the system until $c = c_{st}$ is attained. According to Eq. (30), the effective coefficient of restitution is about 0.63 at $\tau \to 0$, while for $\tau = 1, \varepsilon_{cr} \approx 0.81$. This decrease in the allowed amount of dissipation follows from the reduced local viscous gain as mean free paths are reduced due to increased impact frequency; it also implies that steady-state c_{st} drops with τ. However, for $c/(R\Omega)$ close to unity the nonlocal contribution to viscosity can no longer be ignored. This provides an additional source of energy balancing the dissipation, and prevents the complete flattening of the system into a monolayer. In practice Eq. (29) implies that there is a minimum velocity dispersion $c \propto R\Omega$.

According to Fig. 1, for the Hatzes et. al. formula the low τ critical coefficient of restitution $\varepsilon_{cr} = 0.63$ corresponds to impact velocity $v_n \approx 1.5$ cm/s. For our nominal particle size $R = 1$ m and Saturnocentric distance $a = 100,000$ km ($\Omega = 2 \times 10^{-4}$ s^{-1}) this converts to $c/(R\Omega) \sim 30$. The energy balance is thus dominated by local viscosity at small τ's. On the other hand, for the Bridges et al. formula, the $\varepsilon_{cr} = 0.63$ would imply a very cool state, which contradicts the assumptions which Eq. (30) was based on: therefore the energy balance is expected to be affected by the nonlocal viscosity at all optical depths. A similar situation holds if the coefficient of restitution has a constant value $\varepsilon_n < \varepsilon_{cr}(\tau)$: the system flattens to a near monolayer state, with the minimum velocity dispersion maintained by nonlocal gain (a constant $\varepsilon_n > \varepsilon_{cr}(\tau)$ would lead to dispersal of the system via unbalanced heating).

Results of simulations performed with these elastic models are shown in Figs. 2 and 3. All the runs were made with $N = 500$–4000 particles, and steady-state values are collected for the duration of 100 orbital periods. The calculation regions were large enough to cover particle epicycles and small enough to suppress instabilities. Optical depths in the range 0.01–10 were simulated. The simulations confirm the expectations following from the qualitative Eq. (29). Fig. 2, displaying the effective value of ε_n in simulations, shows that the Hatzes et al. smooth particle model follows the theoretical $\varepsilon_{cr}(\tau)$ relation until $\tau \sim 1$, whereas $\varepsilon_n < \varepsilon_{cr}$ for the Bridges et al. frosty particle model. Related to this, the smooth particle model shows a strong drop in the velocity dispersion c, by a factor of nearly five, as τ increases. For the frosty particle model the drop is less than a factor of 2. Besides the actual velocity dispersion, Fig. 3 shows also the effective c_0, including the contribution from nonlocal pressure: for both models this turns into increase for large τ's. The geometric thickness of the system, measured directly from the particles' vertical dispersion, follows very closely the effective c_0: the increase for larger τ's is due to piling of particles into a multilayer. On the other hand, vertical thickness estimated from c_z (dashed lines) follows closely the total c. The maximum average impact velocities, obtained at the limit $\tau \to 0$ are 1.2 and 0.1 cm/sec for the Hatzes at al. and Bridges et al. formulae, respectively.

Most importantly, the two elastic models lead to a qualitatively different ν versus τ and η versus τ relations (lower frames of Fig. 3). While the frosty particle model implies a monotonically increasing ν due to the nonlocal part, for the smooth particle model the drop

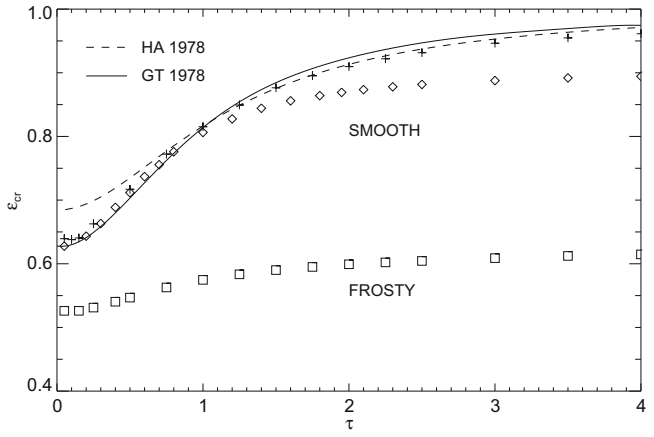

Fig. 2. Theoretical thermal stability boundary ε_{cr} versus τ, according to Goldreich and Tremaine (1978; solid line) and Hämeen-Anttila (1978; dashed line), who used different approximations in the evaluation of the collision integrals. For a constant $\varepsilon > \varepsilon_{cr}(\tau)$ the viscous dissipation is too weak to balance the viscous gain of energy, leading to a rapid dispersal of the ring via increased random velocities. Also shown are the effective steady-state values of ε_n in the simulations performed with the Hatzes et al. (open diamonds; "smooth") and Bridges et al. (squares, "frosty") elasticity models. Note that the 'smooth' particle simulations follow closely the theoretical curves until $\tau \approx 1$, beyond which the nonlocal contribution can not be ignored. On the other hand, the 'frosty' particle simulations fall below theoretical curves for all τ's. Also shown in the plot (crosses) are simulations performed with the Hatzes et al. (1988) "polished ice" model mentioned in the text: for this model the system remains hot, $c \gg R\Omega$, for the whole studied τ interval, and the simulation results are well accounted by the theoretical formula (this dilute 'mass-point' limit approximates the assumptions behind the theoretical curves). The average ε_n in simulations is measured by weighting each impact with the square of the normal component of impact velocity, $\langle \varepsilon_n v_n^2 \rangle / \langle v_n^2 \rangle$.

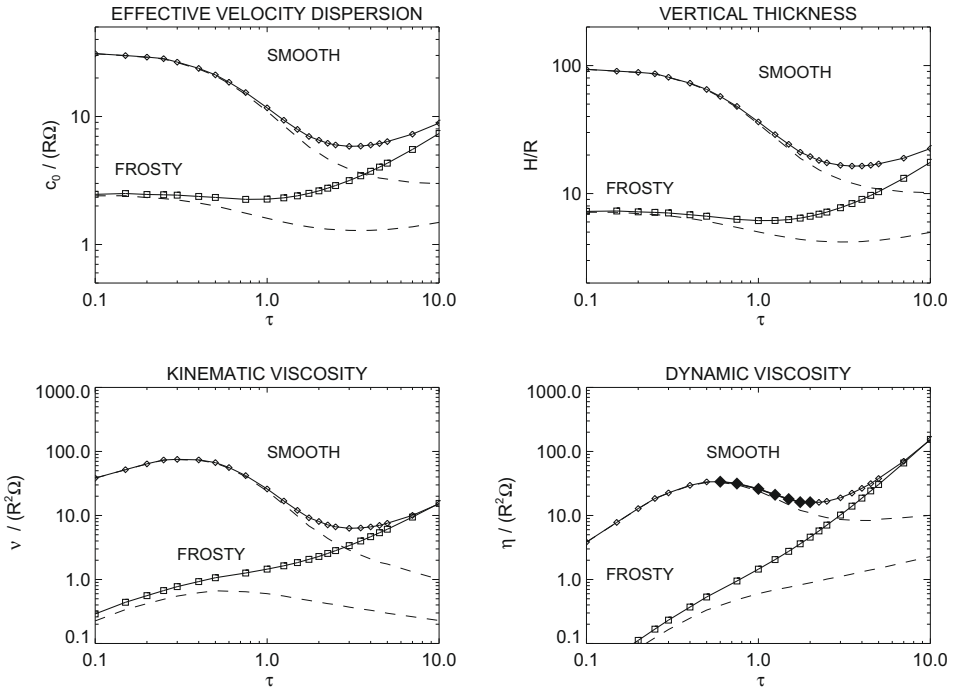

Fig. 3. Steady-state effective velocity dispersion c_0, geometric thickness H, kinematic viscosity ν, and dynamic viscosity $\eta = \nu\tau$ as a function of optical depth, for the two elastic models displayed in Fig. 1. A particle size $R = 1$ m and a Saturnocentric distance of $a = 100,000$ km are assumed. The effective velocity dispersion is defined via the equation $p = c_0^2\tau$ and thus contains the contribution of nonlocal pressure besides the local pressure due to dispersion of particle velocities; velocity dispersion itself is indicated by the dashed curves. The geometric thickness $H = \sqrt{12\overline{z^2}}$ corresponds to the full thickness of a uniform layer which has the same vertical dispersion as the actual distribution. Also shown by a dashed curve is the thickness estimated from the vertical velocity dispersion, $\sqrt{12}c_z/\Omega$; in the case of low filling factor these two measures are identical. However, for flat systems the piling of particles eventually thickens the system although c_z stays almost constant with τ. For the kinematic viscosity ν and dynamic viscosity η the contribution from local viscosity is shown separately with dashed lines. Filled diamonds indicate the τ-regime with negative $\partial\eta/\partial\tau$, susceptible to viscous instability.

in ν_{local} is so strong that it establishes $\frac{\partial\eta}{\partial\tau} < 0$ for an interval $0.6 < \tau < 2$. This difference is further illustrated in Fig. 4, displaying the $\beta(\tau)$ curves of the two models. As discussed above, the basic reason for the existence of the unstable branch is the high velocity dispersion at the limit $\tau \to 0$ implied by the Hatzes et al. type elasticity model, allowing for a strong drop of velocity dispersion when τ increases.

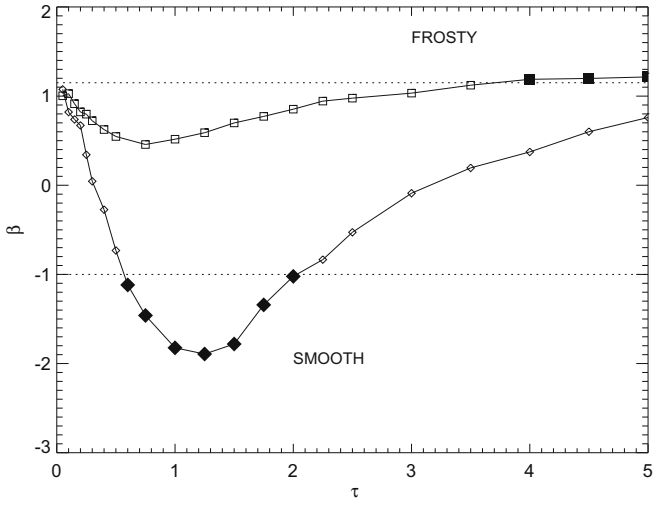

Fig. 4. The slope $\beta \equiv d\log(\nu)/d\log(\tau)$ for the simulations using the two elastic models of Fig. 1. Solid diamonds and squares indicate the regions susceptible to either viscous instability or viscous overstability, respectively.

4. Direct simulations of viscous instability

Fig. 3 (or Fig. 4) suggests that the ground state properties for the *smooth particle* elasticity model fulfill the viscous instability condition for $\tau \sim 1$. Simulations with the Hatzes et al. (1988) elasticity law should thus show this instability, provided that the radial size of the simulation region is large enough to cover the smallest unstable wavelengths, which according to linear stability analysis performed with the measured ν and p (Table 1) are of the order of 100 particle radii. Simultaneously, the tangential size of the calculation region must be large enough to cover the particle epicycles. Taken together, these conditions indicate that at least $N \sim 10^4$ simulation particles are needed in order to verify the viscous instability in direct 3D local simulation. First such attempts were reported already in Salo (1991), using an ad hoc impact law (Bridges et al. type formula, except with $v_c/v_B = 40$ instead of unity; using increased scale factor implies a larger steady-state velocity dispersion, see Salo (1991)), which similarly predicts instability for $\tau \sim 1$. However, since the maximum N attainable in

Table 1
Ground state parameters used in hydrodynamic analysis: Hatzes et al. (1988) elasticity model is used for identical non-gravitating 1 m particles at Saturnocentric distance $a = 100,000$ km.

τ	$\nu_{local}/(R^2\Omega)$	$\nu/(R^2\Omega)$	$c/(R\Omega)$	$c_0/(R\Omega)$	β
0.10	38.3	38.4	30.9	31.0	0.82
0.50	65.8	67.0	20.8	21.1	−0.73
1.00	24.0	26.0	11.0	11.7	−1.82
1.50	9.8	12.0	6.9	7.9	−1.78
2.00	5.5	8.0	5.2	6.5	−1.02
2.50	3.7	6.7	4.3	6.0	−0.53

simulations at that time was only $\sim 10^3$, these experiments were not successful. With the present particle numbers viscous instability is easily simulated.

In this section direct simulations are used for two purposes: for measuring the linear growth rates from simulations, and for following the evolution to the nonlinear regime.

4.1. Comparison of linear growth rates to hydrodynamical theory

In order to measure the linear growth rates we shall impose a small amplitude perturbation to the system and follow its decay or growth with time. To assure that the fastest growing modes do not disturb the measurements, each of the allowed modes with a radial wavelength

$$\lambda = L_{radial}/m, \quad \text{with } m = 1, 2, \ldots \tag{31}$$

is studied in a separate simulation. Typically, we will use simulation regions with radial extent $L_{radial} = 2$ km (2000 particle radii). This is a similar approach to what we applied in our previous growth time measurements for overstable oscillations (Salo et al., 2001; Schmidt et al., 2001; Schmidt and Salo, 2003). However, in the case of oscillatory instability, the excitation of a single mode was easy to achieve, by imposing a sinusoidal perturbation in the mean radial velocity, which corresponds to one of the eigenvectors of the linear solution. Moreover, it posed no problem to add this perturbation during the simulation after the energy balance was achieved, since the particle positions need not be altered. In the case of instability, the velocity amplitudes are extremely small, and we must impose the density perturbation directly in the initial distribution of particles. In practice, radial positions are created in a manner that produces the desired small sinusoidal perturbation in the radial profile, after which particles' tangential coordinates are randomly chosen, except that overlaps are not allowed. Eccentricities and inclinations are chosen according to a Rayleigh distribution. When this procedure is used, there is a short transition period during which the perturbation has already set in, though the system has not yet settled to an equilibrium. However, by choosing the parameter of the Rayleigh distributions as close to equilibrium values as possible, one can minimize the effect of this transition period. Additional checks were also made to assure that the measured growth rates are not affected by the tangential or radial width of the system (comparisons were made with twice larger calculation regions). It was also checked that simulations using the force method gave essentially the same results as the adopted instantaneous impact method (see also Fig. 14 below).

To obtain the growth rates, the Fourier amplitudes of different radial m-components were tabulated as a function of time, for density, mean radial, and mean tangential velocity. A linear fit of the logarithm of amplitude versus time was then performed. The first five periods were excluded from the determination of growth rates. Also, each fit was checked by eye to make sure that the fit range did not extend beyond the linear growth period. In practice, only the density amplitudes were useful, as the velocity amplitudes did not stand above the noise caused by the discreteness of the system.

In Fig. 5 the linear growth rates are compared to hydrodynamical modeling, for four different initial optical depths, covering the suspected unstable range $\tau = 0.6$–2.0. The growth rates are displayed in terms of e-folding times, in the units of orbital periods: $T_e = \Omega/(2\pi \mathrm{Re}(\omega))$. The solid and dashed curves show the prediction of the linear dispersion relation, while the symbols stand for

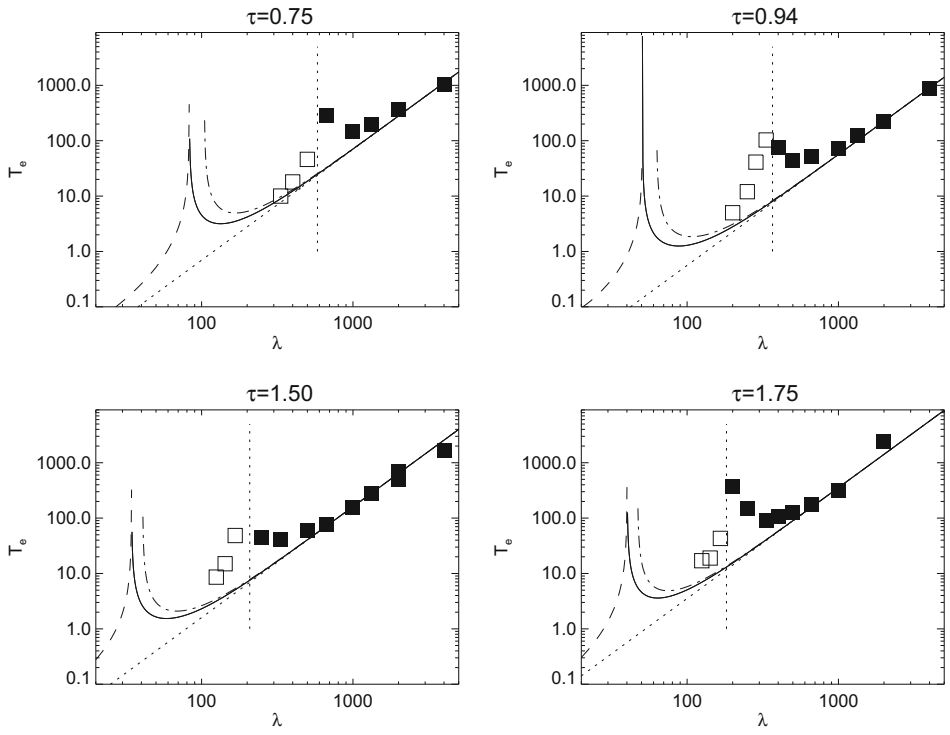

Fig. 5. Comparison of simulated growth rates versus wavelength with those predicted by hydrodynamic stability analysis. The curves indicate the e-folding times following from the dispersion relation Eq. (14), using the pressure and viscosity values measured for the Hatzes et al. smooth particle elasticity model: solid and dashed curves indicate growth and decay, respectively. For the dash-dotted curve, the radial component of the pressure tensor P_{xx} was used instead of the isotropic pressure p; in this case only the unstable branch is shown. Also marked, by a dotted line, is the asymptotic growth rate, Eq. (16). Squares stand for the e-folding times measured in simulations, filled and open boxes corresponding to growth and decay, respectively: each symbol corresponds to a separate simulation where a small seed amplitude was given for the studied mode. The smallest unstable wavelength (interpolated from simulations) is marked with a vertical dotted line. Times are measured in orbital periods and lengths in particle radii (=m). At the long wavelength limit the simulated growth rates are in good agreement with hydrodynamical prediction: however, there is clear discrepancy, by about a factor of almost 10, in the smallest unstable wavelength.

Table 2
Comparison of predicted (HYDRO) and simulated (SIMU) minimum unstable wavelengths, $\lambda_{\min}$, and asymptotic growth rates, $\lim_{\lambda\to\infty} T_e/\lambda^2$ (T_e in orbital periods, λ in kilometers): Hatzes et al. (1988) elasticity model, identical non-gravitating 1 m particles at Saturnocentric distance $a = 100,000$ km.

τ	$\lambda_{\min}$ HYDRO (m)	$\lambda_{\min}$ SIMU (m)	T_e/λ^2 HYDRO	T_e/λ^2 SIMU
0.75	80	580	62	90
0.94	50	370	52	56
1.50	35	210	164	176
1.75	40	180	320	620

the simulated growth rates. The predicted and simulated values for the smallest unstable wavelength $\lambda_{\min}$, and for the asymptotic growth rate $\lim_{\lambda\to\infty} T_e/\lambda^2$, are collected to Table 2. Clearly, there is a considerable difference in the predicted $\lambda_{\min}$, by almost a factor of 10. This difference is roughly the same for all studied optical depths, see Fig. 6. Also shown in these figures are the hydrodynamic predictions where instead of isotropic pressure the radial pressure component is used for the calculation of c_0. Since the velocity ellipsoid is radially elongated we have $P_{xx} > p$, which shifts the predicted unstable regime to somewhat larger wavelengths. The shift is however much too small to account for the difference between hydrodynamic predictions and simulations. The difference is probably in large parts due to the assumption of isothermality in the model: A similar shift of instability to larger wavelengths by non-isothermal effects was observed for viscous overstability (see Fig. 4 in Schmidt et al., 2001). Altogether, the exact interpretation of hydrodynamic pressure is problematic: for example, had we used the difference of ground state pressures to estimate the $\partial p/\partial\tau$ instead of using $c_0^2 = p/\tau$, we would have predicted even smaller unstable wavelengths and larger growth rates. On the other hand, the growth rates at the large-wavelength limit are in good agreement with the hydrodynamic prediction, depending only on the measured ν_0 where there is no such ambiguity.

4.2. Spontaneous growth and saturation to nonlinear steady-state

To follow the spontaneous growth of instabilities and their evolution beyond the linear amplitude regime, additional large scale simulations with the Hatzes et al. (1988) elasticity model were performed for several different τ's. No initial perturbation was applied, so the instability, if present, arose from random noise. Fig. 7 shows the time evolution of the radial density profile for systems with different initial uniform optical depths, and Fig. 8 displays the final profiles in the end of each run (1500 orbital periods). In agreement with the linear stability analysis, the run with $\tau = 0.5$ is stable, whereas runs with $\tau = 0.75,\ 1.0,\ 1.5$ are unstable, leading to a formation of ringlets with a distinctly non-sinusoidal flat-top profiles. The separation of ringlets gets smaller with τ, in accordance with Fig. 5, which indicates that the wavelength of the mode with the largest linear growth rate is reduced from about 1000 m to 300 m in this τ interval. Increasing the optical depth to $\tau = 1.9$ also leads to instability, but now rather than forming separate ringlets, the system develops a couple of lower optical depth regions. At $\tau = 2.0$ the system is very close to the linear stability boundary, developing just small amplitude perturbations. At still larger τ's the system remains completely stable.

We study in more detail a system with $\tau = 0.94$. This optical depth is chosen since it yields the fastest asymptotic growth rate (both according to simulations and hydrodynamic analysis, see Fig. 6). Starting with a uniform profile the system with a radial width of 2 km divides into four distinct ringlets during the first 100 orbital periods (Fig. 9). After about 200 periods, the leftmost ringlet has clearly saturated to a practically constant level. However, the second ringlet from the right, after an initial growth has started to disperse again, the material apparently being captured by the two adjacent ringlets which are slowly growing and shifting toward the dispersing ringlet. As suggested by Fig. 7 this process will eventually lead to merging of the ringlets. Fig. 10 displays the system after 500 orbital periods: the ringlets have a distinctly lower vertical thickness and velocity dispersion than the inter-ringlet regions. This is in accordance with the notion of instability leading to a bimodal state with a co-existence of hot low density and cool high density regions (Hämeen-Anttila, 1982).

To analyze the non-linear steady-state reached in the above simulation, Fig. 11 displays the radial profiles of dynamic viscosity and isotropic pressure. These profiles are constructed by tabulating the pressure tensor components at different radial zones of the system, and averaging over 50 orbital periods. This figure (uppermost frame) confirms the expectation that η is constant in the steady-state: this seems to be the case except for the decaying ringlet, which corresponds to a local maximum of η. Note that both the local and nonlocal viscosities have a significant contribution to the total viscosity, depending on the location: at the rarefied regions between ringlets the viscosity is almost solely due to local component, while at the ringlets both components have about the same magnitude. On the other hand, the pressure (lower frame in Fig. 11) is not constant, having a lower than average value near the ringlet edges. Again, for the ringlets the local and nonlocal components are both significant. To balance the implied pressure gradient the mean tangential velocity must adjust accordingly.

Fig. 12 checks for the validity of the momentum balance equations at the non-linear steady-state, using the same tabulation interval as in Fig. 11. The upper frame compares the simulated mean tangential velocity v, with that calculated from the gradient of P_{xx}, using the hydrodynamic balance equation for radial momentum. For steady-state $\frac{\partial u}{\partial t} \approx 0$, and Eq. (4) implies

$$v \approx \frac{1}{2\Omega\tau}\frac{\partial P_{xx}}{\partial x}. \tag{32}$$

An excellent agreement is found, providing a useful check of both the pressure tensor tabulation method, as well as for the applicability of the kinetic equations themselves in describing these discrete particle systems. According to this figure, the shear is slightly reduced at the edges of the ringlets ($\frac{\partial v}{\partial x} > 0$) and enhanced

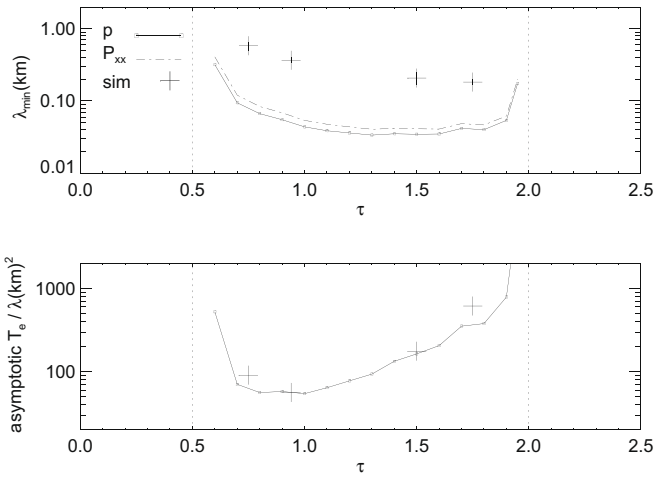

Fig. 6. The upper frame compares the minimum unstable wavelength predicted by the hydrodynamical analysis (curves) with those obtained in simulations (symbols). The solid curve uses the isotropic pressure $p = \frac{1}{3}trP$, while the dash-dotted curve indicates the change if p is replaced with the P_{xx} component. In the lower frame the asymptotic large wavelength e-folding times are compared, indicating a good agreement; note that the theoretical curve depends only on kinematic viscosity. Vertical dotted lines roughly indicate the stability boundaries found in simulations, matching well with the hydrodynamic prediction.

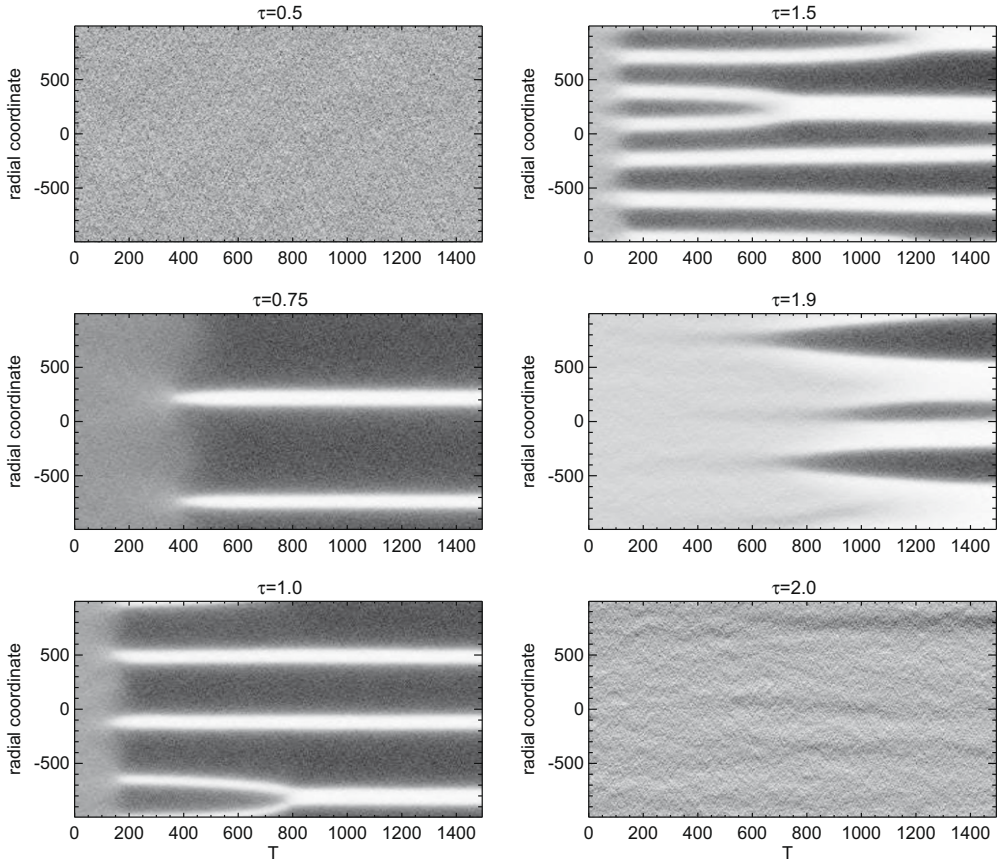

Fig. 7. Time evolution in simulations using the Hatzes et al. smooth particle elasticity model. Six simulations starting from different initial optical depths are compared. The tangential and radial widths of the simulation system were fixed to 40 and 2000 particle radii (=m), and the different optical depths correspond to $N = 13{,}000$–$50{,}000$ simulation particles. The horizontal axis indicates the time measured in orbital periods, and the vertical axis corresponds to the radial coordinate measured in meters: the tangentially averaged number density was stored every five orbits, using 200 radial bins. Grey-scale indicates the number density, white corresponding to density enhancement. For absolute scales see Fig. 8, displaying the radial τ profiles in the end of these runs.

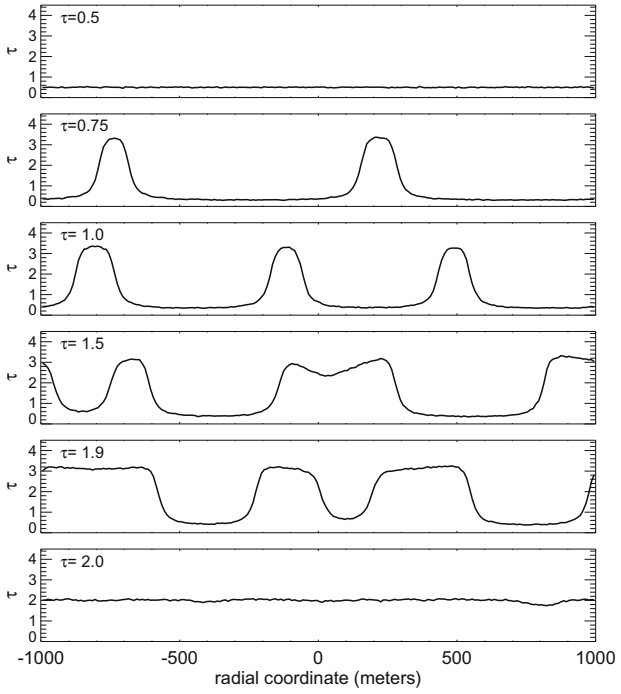

Fig. 8. The radial density profiles of the simulations displayed in Fig. 7, averaged between 1400 and 1500 orbital periods. The initial uniform optical depth is indicated on each frame.

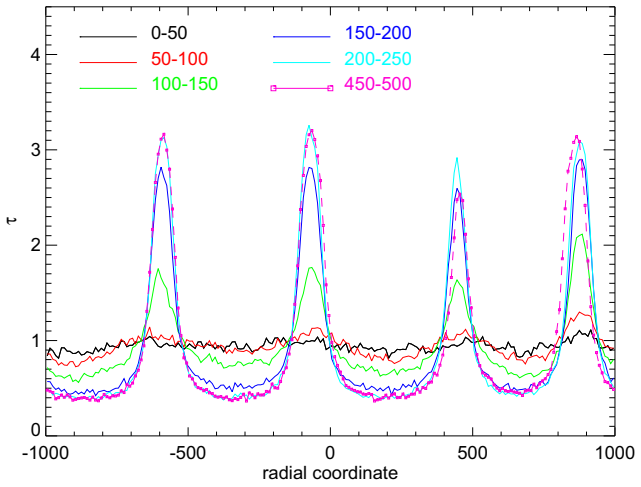

Fig. 9. The time evolution of the radial profile for an unstable simulation system, using the Hatzes et al. smooth particle elasticity model. In the initial state 24,000 particles were uniformly distributed in a calculation region with radial and tangential widths of 2000 and 40 particle radii (=m), and optical depth $\tau = 0.94$; this τ corresponds to the largest asymptotic linear growth rate. The solid lines, in the order of increasing peak value, show the profile averaged over orbital periods 0–50, 50–100, 100–150, 150–200 and 200–250, while the dashed line with symbols indicates the profile for orbits 450–500. Note that the density of the two leftmost ringlets has saturated to an almost constant level, while the second ringlet from the right has started to disperse, the material being captured mainly by the rightmost ringlet which is slowly growing and shifting toward the dispersing ringlet.

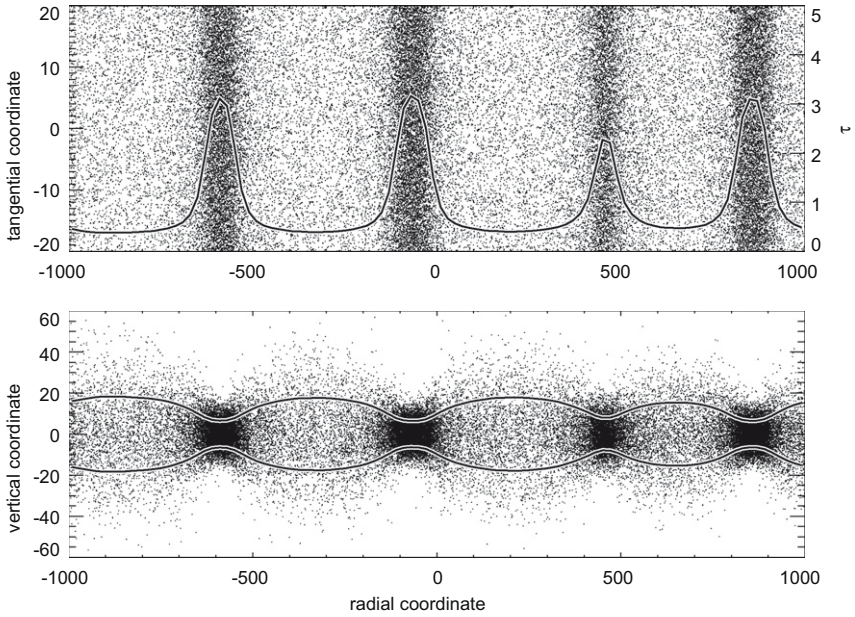

Fig. 10. Snapshot of the simulation displayed in Fig. 9, after 500 orbital periods. Both a projection to the equatorial plane and a side view along the tangential direction are shown; note that the vertical scale is exaggerated by a factor of five. Solid lines indicate the optical depth profile (upper frame) and the vertical dispersion ($\pm\sqrt{\overline{z^2}}$) profile (lower frame). The velocity dispersion is proportional to vertical dispersion.

between them ($\frac{\partial v}{\partial x} < 0$), compared to the Keplerian shear gradient $-\frac{3}{2}\Omega$. However, the maximum deviation from Keplerian profile is about 0.3%. The lower frame of Fig. 12 shows a similar check for the tangential momentum balance. With $\frac{\partial v}{\partial t} \approx 0$ Eq. (5) implies

$$u \approx -\frac{2}{\Omega\tau}\frac{\partial P_{xy}}{\partial x}. \tag{33}$$

The agreement indicates that the very small residual radial velocities present in the system are in accordance with the gradients of P_{xy}. In particular, the positive $\frac{\partial u}{\partial x}$ gradient at the ringlet around $x \sim 500$ is related to gradual flow of particles away from this ringlet.

Finally, Fig. 13 shows the radially tabulated quantities at the nonlinear steady-state, plotted against the optical depth at the same radial bin, with those measured for the uniform ground state.

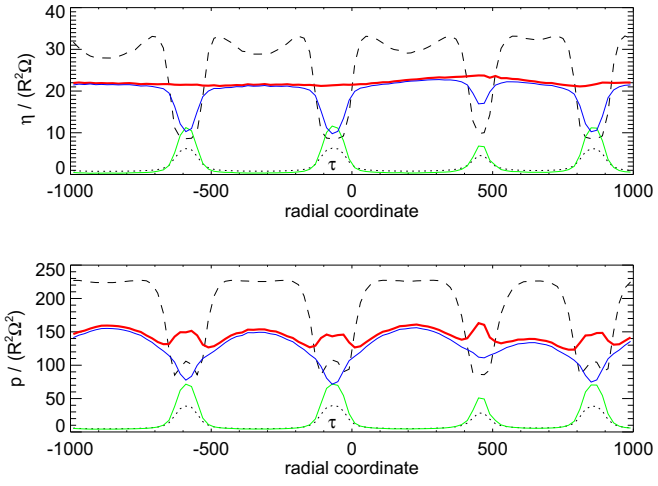

Fig. 11. Upper frame: the thick red line shows the dynamic viscosity profile for the simulation displayed in Fig. 10. Also shown, by dashed lines, is the ground-state value of the dynamic viscosity which would correspond to the local τ in each radial zone. Note that the dynamic viscosity in the simulation is almost constant, except for the dispersing ringlet (second one from the right); here a local maximum is seen, consistent with the particle flow directed away from this radial zone. The local and nonlocal contributions to η are shown separately by the blue and green thin solid curves, respectively (nonlocal contributions peak at the ringlets). Dotted lines indicate the optical depth profile (in arbitrary units). Lower frame: similar profiles for the isotropic pressure. Note that the total pressure is not constant. To obtain these profiles, the local and nonlocal pressure tensors were tabulated in 100 radial zones, and averaged over 50 orbital periods (orbits 500–550). (For interpretation of the references to colour in this figure legend, the reader is referred to the web version of this article.)

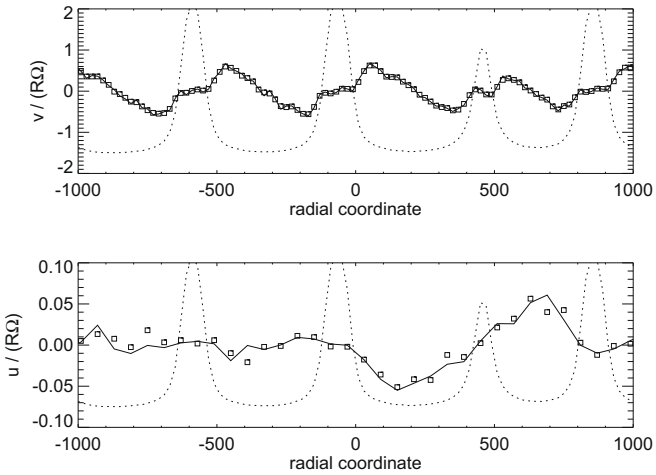

Fig. 12. Check of the hydrodynamic balance equations for the simulation displayed in Fig. 10. Upper frame: the radial momentum balance. The solid line shows the tangential mean velocity $v = \overline{y} + \frac{3}{2}\Omega\overline{x}$, maintained by the gradient in the radial component of pressure tensor. Symbols indicate $\frac{1}{2\tau\Omega}\frac{\partial P_{xx}}{\partial x}$ in units of $R^2\Omega^2$; the overlap with tangential velocity indicates that Eq. (4) with $\frac{\partial u}{\partial t} = 0$ is accurately fulfilled. Lower frame: the tangential momentum balance. The solid line shows the radial velocity profile $u = \dot{\overline{x}}$, while symbols display $-\frac{2}{\tau\Omega}\frac{\partial P_{xy}}{\partial x}$; the overlap indicates that Eq. (5) with $\frac{\partial v}{\partial t} = 0$ is fulfilled. Note that the dispersing ringlet has a positive gradient $\frac{\partial u}{\partial x} > 0$, which according to continuity equation indicates reduction of density. Also shown in both frames is the optical depth profile (dotted curve, arbitrary scale). To obtain these profiles, the local and nonlocal pressure tensors, together with mean velocities and densities were tabulated in 100 radial zones, and averaged over 50 orbital periods (orbits 500–550).

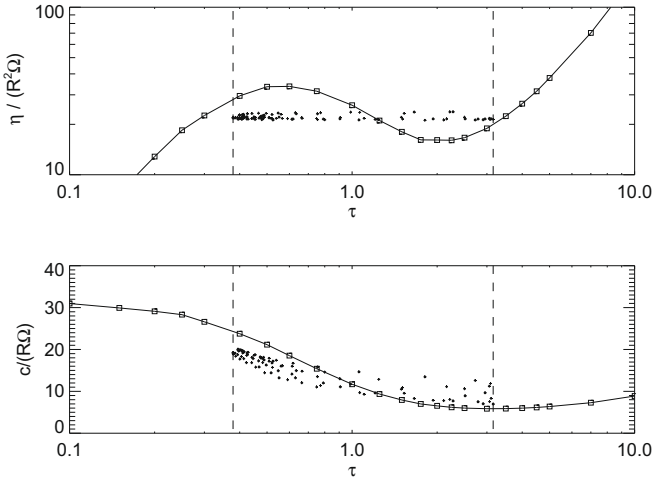

Fig. 13. Properties of nonlinear steady-state. Upper frame: the solid curve indicates the ground-state dynamic viscosity η as a function of τ, evaluated in separate simulations whose radial scale was chosen small enough to suppress the instability (same curve as in Fig. 3). The symbols show the same quantity evaluated for different radial locations of the large-scale simulation in Fig. 10, plotted against the optical depth in the same radial location. Lower frame: Same for radial velocity dispersion. Note that the nonlinear steady-state values differ from the ground-state values.

Since the simulated $\eta(x)$ is constant, considerable difference are seen in comparison to $\eta_0(\tau(x))$. For example, using the ground state $\eta_0(\tau)$ curve to estimate the low τ value needed to balance the maximum $\tau_{max} \approx 3$ would suggest $\tau_{min} \approx 0.3$, instead of the simulated $\tau_{min} \approx 0.4$. On the other hand, for $c_x(x)$ the deviations from ground state $c_x(\tau(x))$ are quite small.

4.3. Viscous instability and self-gravity

The ST1995 hydrodynamic dispersion relation includes the effects of axisymmetric self-gravity: for example, in the absence of pressure and viscous terms it leads to the Toomre (1964) stability criterion $Q > 1$ for the linear stability against the growth of axisymmetric gravity perturbations. For viscous instability, the dispersion relation predicts that axisymmetric gravity leads to enhanced growth rates and to somewhat smaller minimum unstable wavelength (See Fig. 1 in ST1995).

A convenient way for rapid inclusion of axisymmetric self-gravity to simulations is provided by the same method which was utilized in the hydrodynamic analysis. We make a radial Fourier decomposition of the tangentially averaged surface density,

$$\sigma(x) = \sigma_0 \left[1 + \sum_{m=1}^{\infty} A_m \cos\left(m \frac{2\pi}{L_{radial}} (x - x_m) \right) \right], \tag{34}$$

where σ_0 is the mean surface density, A_m and x_m are the fractional amplitude and phase of different m-components with wavelengths $\lambda = L_{radial}/m$. We then treat each component as an infinite plane wave, and use Eqs. (11) and (12) to calculate the corresponding radial force. Superposition of different modes gives

$$F_x(x) = -2\pi G \sigma_0 \sum_{m=1}^{m_{max}} A_m \sin\left[m \frac{2\pi}{L_{radial}} (x - x_m) \right]. \tag{35}$$

A finite m_{max} is used in order to suppress small scale noise: we include only components corresponding to wavelengths > 20 m.

Although no systematic comparisons of the growth rates were performed, the prediction of enhanced growth rates seems to be consistent with our numerical experiments which include axisymmetric gravity (Fig. 14). In these simulations we apply the same Hatzes et al. elasticity model as before, but use the force method for impact calculations instead of the instantaneous impact method: the first two frames of Fig. 14 verify that in the non-gravitating case the two impact calculation methods give essentially the same results. The third frame shows the time evolution of the density profile with the inclusion of axisymmetric gravity: for the studied parameters the hydrodynamic analysis predicts a nearly 2-fold growth rate with the inclusion of gravity, qualitatively consistent with the clearly faster emergence of ringlets in this case. Also the number of initially formed ringlets is larger, in qualitative agreement with the reduced minimum unstable wavelength predicted by hydrodynamic analysis.

Fig. 14 (lower frame) also indicates what happens when full self-gravity is taken into account, not limiting to the axisymmetric component. Interestingly, although the uniform initial state with $\tau = 1$ is too hot for the self-gravitational wakes to form, these emerge after the viscous instability has lead to the formation of dense cool ringlets with $Q \sim 1$. Due to gravitational viscosity associated with the wakes, the viscosity of dense regions is expected to increase (low-τ regime is not affected), which in principle could destroy the unstable branch of the $\eta(\tau)$ relation: apparently in the shown example the wakes are too weak for this.

5. Comparison to previous particle simulations of viscous instability

5.1. Lukkari (1981) indirect simulations

The principal mechanism behind viscous instability was first simulated in Lukkari (1981), using a computational trick that shifted the region where $\frac{\partial \eta}{\partial \tau} < 0$ to a very low optical depth, of the order of $\tau \sim 10^{-4}$–10^{-3}. In this case the amplification of density fluctuations could be seen in a simulation using a complete ring of just 250 particles (with a radius of 10^{-3} times the mean planetocentric distance), manifesting as an emergence of a single denser ringlet from an initial smooth density distribution. The shift of the unstable τ-regime was achieved by choosing the coefficient of restitution to depend *explicitly* on optical depth, instead of the implicit τ dependence following via the energy balance equation. The formula used was

$$\varepsilon_n(v_n, \tau) = \frac{1}{k(\tau^3 + \tau_0^3) v_n/(R\Omega)}, \tag{36}$$

where $k = 1.91 \times 10^9$, $\tau_0 = 0.752 \times 10^{-4}$, and v_n denotes the impact velocity. For the mean optical depth of the system, $\tau \approx \tau_0$, the low optical depth critical coefficient of restitution, $\varepsilon_{cr} \approx 0.63$, corresponds to $v_n/(R\Omega) \approx 300$, indicating a very hot steady-state. On the other hand, the expected steady-state is much cooler already for a slightly increased τ: for example, inserting $\tau = 10\tau_0$, $v_n/(R\Omega) = 2$ corresponds to $\varepsilon_n \sim 0.4$, consistent with the assumed cool state. Thus, although achieved by an entirely artificial method, the qualitative characteristics of the instability are correctly described, i.e. the particle flux from the higher density, low velocity dispersion regions is balanced by the flux from the surrounding regions with lower density but high velocity dispersion.

5.2. Viscous instability in 2D simulations

Another qualitative demonstration of viscous instability was provided in Salo (2001), in terms of a *two-dimensional* local simulation, with a constant coefficient of restitution close to unity. This also leads to $\frac{\partial \eta}{\partial \tau} < 0$ in a low optical depth regime, making the instability very easy to simulate. However, in comparison to Lukkari (1981) method, this low optical depth instability now follows in a

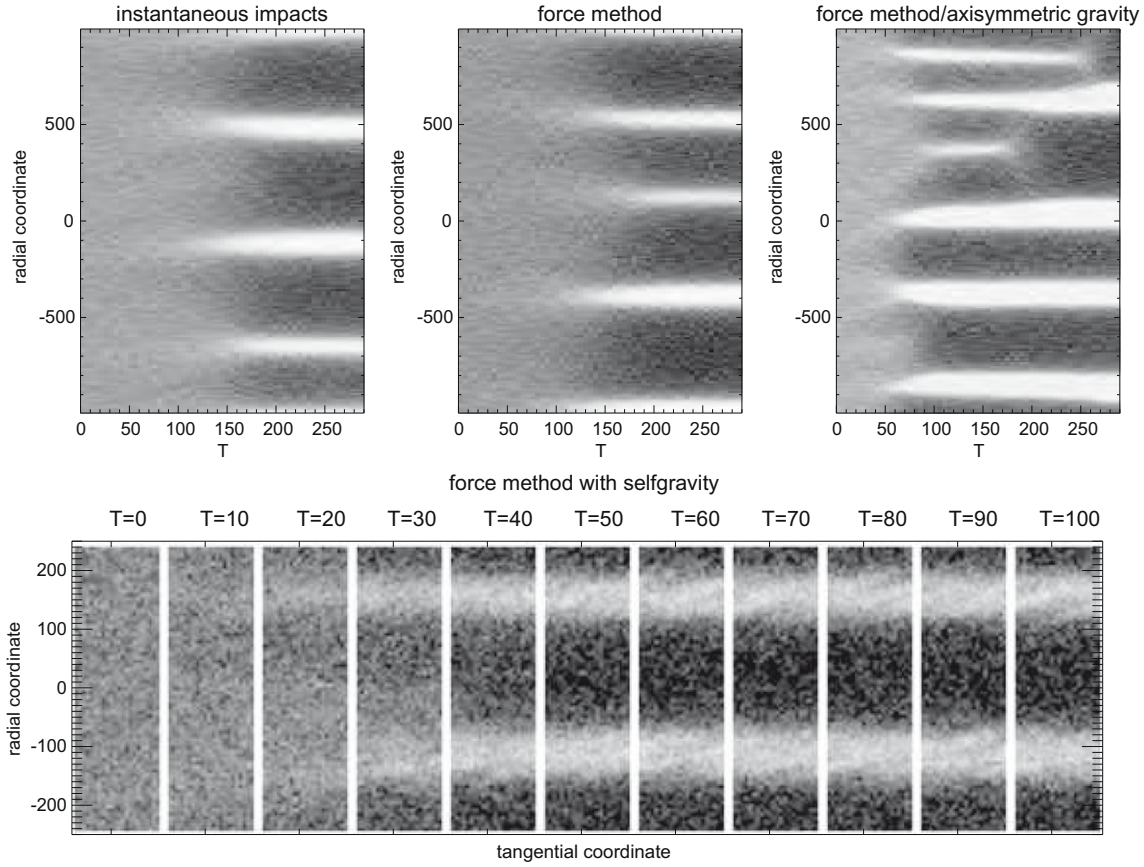

Fig. 14. Viscous instability with the inclusion of self-gravity. The first two frames in the upper row compare simulations performed with the instantaneous impact and force methods: in both cases the Hatzes et al. 'smooth particle' elasticity model is used, for a system with initial optical depth $\tau = 1$. The third frame shows an otherwise similar simulation except that axisymmetric self-gravity is included: the surface density $\sigma = 600\ \mathrm{kg/m^2}$. In all cases a 2000 m (radial) by 40 m (tangential) simulation region was used. In the lower row the full self-gravity is included, using internal particle density $\rho = 450\ \mathrm{kg/m^3}$ (with $\tau = 1$ and $R = 1$ m this corresponds to $\sigma = \frac{4}{3}\rho\tau R = 600\ \mathrm{kg/m^2}$). The size of the simulation region is now 500 m by 160 m: a sufficiently large tangential width (Toomre's critical wavelength is about 42 m) is essential to allow for the nonaxisymmetric wake structure to develop. Snapshots of the system at every 10 orbital periods are shown (horizontal and vertical axis correspond to tangential and radial direction, respectively). The number of simulation particles is ~25,000 in each case.

'natural' way from the different dynamical characteristics of the 2D system in comparison to a realistic 3D case.

The main reason is the different functional dependence of the 2D impact frequency in comparison to the 3D case. The basic formula for impact frequency is $\omega_c \sim n_s c \sigma_c$, where n_s is the space number density, c is the 1D velocity dispersion and σ_c denotes the collisional cross-section. In the 3D-case $\sigma_c = 4\pi R^2$ and $n_s \sim n/H = \tau/(\pi R^2 H)$ where n is the surface number density and H is the vertical thickness. Due to collisional partitioning of energy between vertical and horizontal motions, $H \propto c/\Omega$. The explicit n_s and c dependencies in ω_c thus cancel out and we get the familiar result that ω_c depends solely on τ. A good approximation is provided by

$$\omega_c^{3D} \approx 3\tau\Omega. \tag{37}$$

On the other hand, in the 2D case there is no such adjustment of space density via velocity dispersion, so that impact frequency retains the explicit velocity dispersion dependence. Inserting $\sigma_c = 2R$ yields the formula

$$\omega_c^{2D} \sim \frac{c}{R\Omega}\tau\Omega. \tag{38}$$

A direct consequence of this functional dependence is that in 2D systems dissipation (provided that particles are not totally elastic) is always able to balance the viscous gain, i.e. the critical coefficient of restitution is $\varepsilon_{cr} \equiv 1$ (Salo, 2001). To see this, consider the simple formulas for viscous gain introduced in Section 3,

$$v_{local} = k_2 \frac{c^2\omega_c}{\omega_c^2 + \Omega^2},$$
$$v_{nl} = k_3 \omega_c R^2,$$

where we have now retained the original impact frequency dependence following from the mean free path argumentation. Inserting these to the energy balance equation, and dividing by $\omega_c c^2$ gives the condition

$$1 - \varepsilon_n^2 = \frac{9}{4k_1}\Omega^2 \left(\frac{k_2}{\omega_c^2 + \Omega^2} + k_3 (R/c)^2 \right). \tag{39}$$

In the 3D case ω_c is determined solely by τ, and the above equation has no solution if

$$1 - \varepsilon_n^2 < \frac{9k_2}{4k_1} \frac{\Omega^2}{\omega_c^2 + \Omega^2}, \tag{40}$$

which after substituting ω_c^{3D} leads to the Goldreich–Tremaine formula (30) for ε_{cr}. However, in the 2D case any nonzero $1 - \varepsilon_n^2$ can be balanced for a fixed τ simply by increasing the ω_c^{2D} via increased velocity dispersion. Inserting the 2D formula for impact frequency into Eq. (39) and assuming $c/(R\Omega) \gg 1$ and $\omega_c/\Omega \gg 1$ (appropriate for small $1 - \varepsilon_n^2$), gives the relation

$$1 - \varepsilon_n^2 \propto \left(\frac{R\Omega}{c} \right)^2 \frac{1}{\tau^2}. \tag{41}$$

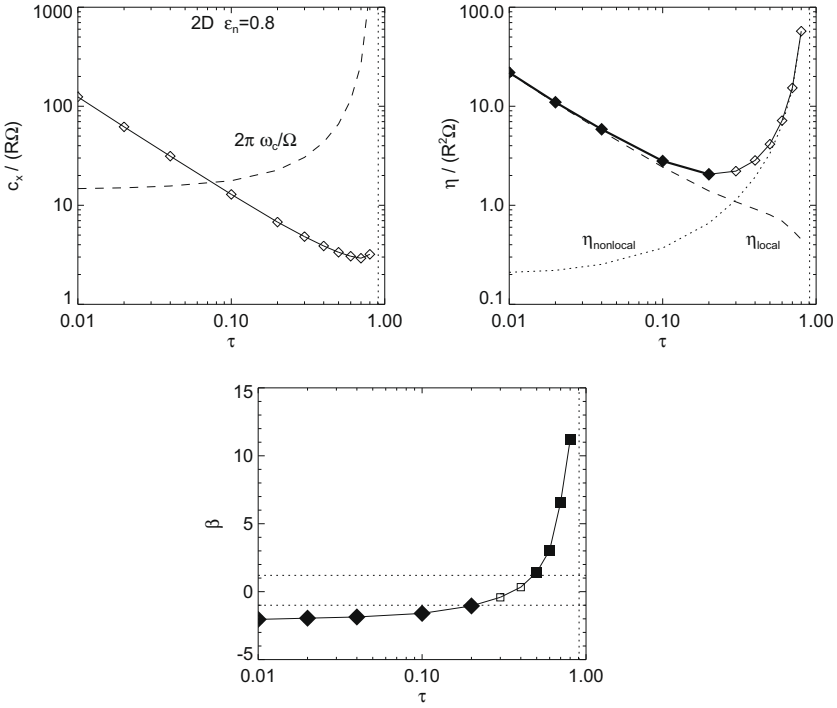

Fig. 15. Ground state properties in two-dimensional simulations with a constant coefficient of restitution $\varepsilon_n = 0.8$. In the upper left, the radial velocity dispersion c_x and impact frequency ω_c are shown as a function of optical depth ($2\pi/\Omega \times \omega_c$ gives the number of impacts/particle/orbital period). The dotted vertical line indicates the 2D maximal packing limit $\tau \approx 0.907$. In the right, the dynamic viscosity η is displayed; also shown separately are the contributions from local and nonlocal viscosities. The thick portion with filled symbols indicates the unstable regime, extending in the 2D case from arbitrarily small optical depth to $\tau \approx 0.2$. The lower frame shows the slope $\beta \equiv d\log(\nu)/d\log(\tau)$: solid diamonds and solid squares indicate the regions susceptible to either viscous instability or viscous overstability, respectively.

For a fixed ε_n this implies $c \propto 1/\tau$. Consequently, at low τ we have $\nu \approx \nu_{local} \sim c^2/\omega_c \propto \tau^{-2}$. Thus $\eta = \nu\tau \propto \tau^{-1}$ and the condition for viscous instability is fulfilled by an ample margin. What is effectively taking place is that the mean free path reduction due to frequent impacts, which in the realistic 3D case requires $\tau \sim 1$, is now taking place for any nonzero τ.

The above qualitative considerations are verified in Fig. 15 in terms of two-dimensional particle simulations using a constant $\varepsilon_n = 0.8$. In the left, the steady-state velocity dispersion and impact frequency are shown, confirming the $c \propto 1/\tau$ and $\omega_c \propto c\tau \approx const$ trends at low τ. This leads to viscosity dominated by $\nu_{local} \propto \tau^{-2}$. When optical depth increases beyond about 0.2–0.3, and in particular when it approaches the maximum 2D value $\tau_{max} = \pi/\sqrt{12} \approx 0.91$, the impact frequency starts to grow in a very nonlinear fashion, leading to a rapidly increasing ν due to strong nonlocal viscosity. As a consequence, the resulting $\eta_0(\tau)$ curve predicts that all $\tau \leqslant 0.2$ should be unstable, whereas for $\tau > 0.2$ viscous instability should be avoided.

Examples of 2D viscous instabilities in larger scale simulations are shown in Fig. 16. The plot shows the radial density profiles as a function of time up to 1500 orbital periods. For $\tau = 0.025, 0.05,$ and 0.10 the onset of instability is very fast: in about 50 orbital periods the system has divided into separate ringlets, which then gradually merge together. Clearly this merging will proceed with time provided that it is not prevented by the small size of the system. For $\tau = 0.20$, close to the predicted linear stability boundary, the emergence of instability is substantially slower, and leads at first to a few density depletions rather than separate ringlets. In this sense the evolution resembles the 3D example with $\tau = 1.9$. However, in the 2D simulation the depletions rapidly clear into gaps which widen with time, eventually leading to distinct ringlets. This different behavior is in accordance with the different ground state $\eta_0(\tau)$ relation. Like in the 3D case, the 2D simulation system tries to adjust $\eta(r)$ to a constant value throughout the system. However, an important difference is that now all low optical values are unstable, leading to a continuous clearing of the gaps. Since this increases the dynamic viscosity of gaps, the ringlets must contract in order to maintain the balance. The ringlets seen in Fig. 16 all have $\tau \sim 0.6$ while for the gaps $\tau \sim 0.001$—0.01.[2] For comparison, in the 3D steady-state the low and high optical depth regions ($\tau_{min} \sim 0.5,\ \tau_{max} \sim 3$) are both in the stable branches of the $\eta_0(\tau)$ curve. Increasing the optical depth further beyond 0.2 suppresses the 2D instability: the simulation with $\tau = 0.30$ is definitely stable, in accordance with hydrodynamic prediction.

To look in more detail at the slow merging evolution of ringlets, the right hand side of Fig. 16 shows the time evolution in a simulation which is similar to the $\tau = 0.05$ simulation in the left, except that it has 5-fold radial extent. In Fig. 17 we display ΔL, the mean spacing between ringlets versus time, calculated by dividing the radial width by the number of ringlets (between individual mergings this number stays constant). The data seem to be well fitted by a power law $\Delta L \propto [T - T(0)]^k$, with $k \approx \frac{1}{2}$ expected for a process driven by viscous forces. Some ambiguity is caused by the choice of $T(0)$: the figure shows the data fits for both $T(0) = 50$ and $T(0) = 0$ orbits, giving $k = 0.47$ and $k = 0.59$, respectively (formal errors in the fitted slopes are smaller than the difference). Based on Fig. 16 the choice $T(0) \sim 50$ seems quite reasonable: at this time the distinct ringlets have just about emerged from the background noise.

An interesting detail is the internal dynamics of the high optical depth ringlets formed via viscous instability. In the 2D simulations their $\tau \sim 0.6$ is so high that the ground state $\eta_0(\tau)$ curve in Fig. 15

[2] In practice the small τ regions have such a large velocity dispersion, $c/R\Omega > 100$ that the finite size of the calculation region might limit the maximum contrast achieved.

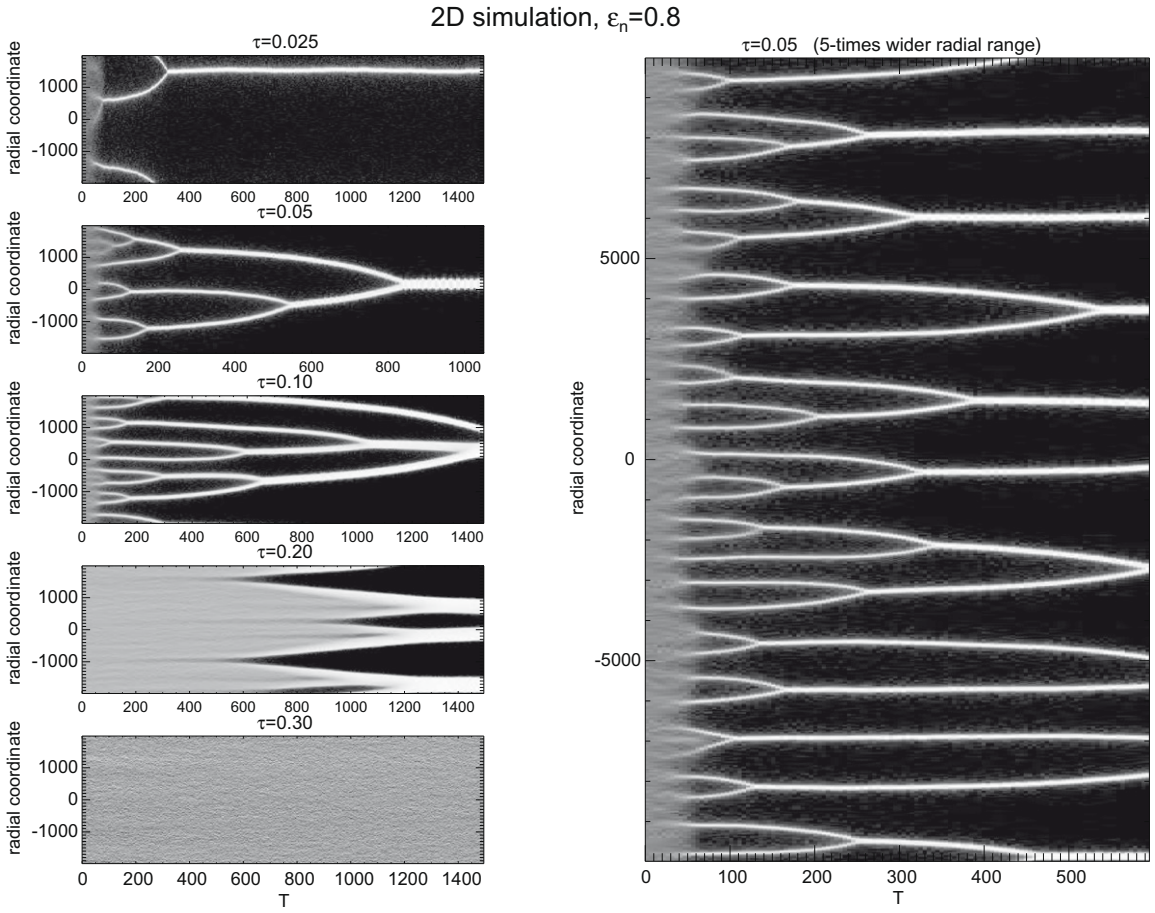

Fig. 16. Comparison of two-dimensional runs for different optical depths. On the left, the evolution of the radial density profile versus time is compared for different optical depths: $\tau = 0.025$, 0.05 and 0.1 are all on the unstable branch, $\tau = 0.2$ is just at the borderline, while $\tau = 0.3$ falls on the stable branch of Fig. 15. The radial and tangential size of the calculation region are 4000 and 62.5 particle radii (=m), and the different τ's correspond to 3200–24,000 particles. On the right, the evolution of a system with $\tau = 0.05$, having a radial and tangential extent of 20,000 and 125 particle radii, respectively; the number of particles is 40,000.

implies $\beta \gg 1$. Since the conditions for obtaining overstability (β_{cr} about unity or slightly larger) is about the same in 2D and 3D simulations (Salo, 2001), this would suggests overstability. However, this estimate of β_{cr} was based on simulations with radially extended systems having periodic boundary conditions: it is not clear whether the same condition applies to a narrow ringlet surrounded by practically empty gaps. Nevertheless, the simulated 2D dense ringlets show clear signs of low amplitude overstable oscillations (Fig. 18). This suggests that the overstable waves are not damped at the ringlet boundaries but are able to reflect back (Papaloizou and Lin, 1988; see also Longaretti and Rappaport, 1995). In principle, overstability would be expected to take place in a similar manner in very dense 3D ringlets: however the $\tau_{max} = 3$ of our simulated 3D ringlets is not yet high enough to lead to overstability (see Fig. 4).

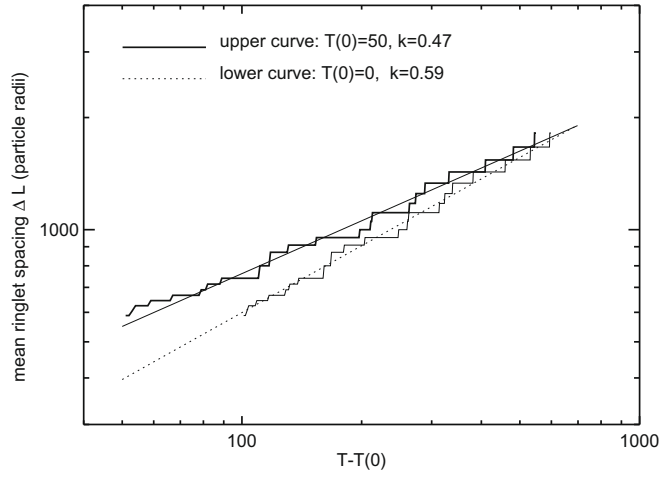

Fig. 17. The average spacing between ringlets in the 2D simulation with 20 km radial width, displayed on the right panel of Fig. 16. The average spacing ΔL is counted by dividing the total radial width of the simulation region by the number of separate ringlets. The data points start from $T = 103$ (times measured in orbital periods), when the first merging of two ringlets occurs. Power law fits of the form $\Delta L \propto [T - T(0)]^k$ are also shown, with two different choices for the zero point of time.

6. Discussion: possible relevance of viscous instability for Saturn's rings

The viscous instability, in some form or another, is in principle a very attractive mechanism when an explanation for the structures in Saturn's ring is sought for: most importantly it would explain naturally the bimodality and the very sharp optical depth transitions seen in the B ring. However, the above hydrodynamic analysis and simulation examples of 3D instability all rely on assuming rather elastic particles, in the sense that $\varepsilon_n > \varepsilon_{cr}(\tau \to 0) \approx 0.63$ for impact velocities $v_n < 1 - 2$ cm/s (this velocity range is set by the minimum velocity dispersion maintained by nonlocal viscosity among meter-sized particles). This enables a hot, many particle

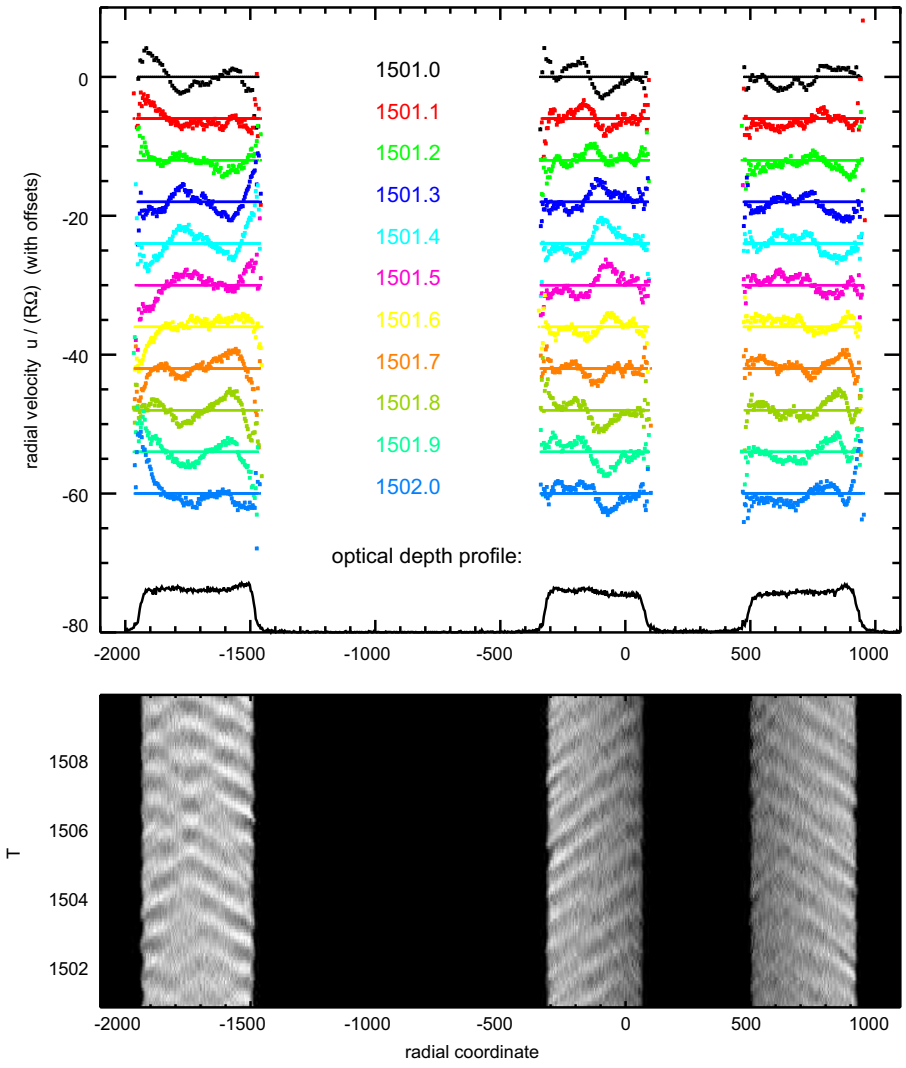

Fig. 18. Overstable oscillations inside the ringlets formed via 2D instability. Upper frame: The evolution of radial velocity profile in the $\tau = 0.2$ simulation of Fig. 16 is followed for one orbital period (1501–1502 periods). For clarity, only the profile for dense ringlets is shown: the τ profile is displayed in the lower axis (for the ringlets $\tau \approx 0.6$). The lower frame displays the evolution of density profile over 10 orbital periods: the gray-scale scale extends $\tau = 0.4$—0.7 (from black to white). The leftmost ringlet shows a superposition of left and right traveling oscillations, whereas the other two are dominated either by right or by left traveling waves.

thick, low τ steady-state, allowing for a sufficiently strong drop of velocity dispersion with density that makes $\frac{\partial \eta}{\partial \tau} < 0$ for intermediate values of τ. At still larger τ the system, now only a few particle thick, is stabilized by nonlocal viscosity. This assumption of rather elastic particles appears implausible, since it would tend to suppress the gravity wake structure known to exist in the A and also in the B ring (Colwell et al., 2006, 2007; Hedman et al., 2007).[3] Note however that we are implicitly assuming that the ring particles have everywhere an effective size $\sim$1 m: actually what is required for the instability to occur is that the ratio $v_c/(R\Omega)$ is sufficiently large. For example, even the Bridges et al. type formula would allow instability if particles in some region had size less than about 2.5 cm.

In any case, other mechanisms for making $\frac{\partial \eta}{\partial \tau}$ negative should be looked for. For example, we have so far not considered the gravitational viscosity, which in the presence of strong self-gravity wake structures is likely to be the dominant source of viscosity (Daisaka et al., 2001). In this case, the expected $\nu \propto \sigma^2$, promoting overstability rather than instability (Salo et al., 2001). However, one might speculate that at extremely high optical depths, there is perhaps no room for the wakes to form: in this case the torque by the inclined wakes is strongly suppressed, which could in principle lead even to a drop of viscosity with increasing τ. To date we have not seen any indication of such behavior in any of our self-gravitating simulations, some of which extend up to optical depths $\tau = 5$.

When looking for possible generalizations of viscous instability, one should also inspect effects that tend to enhance local viscosity at low optical depth relative to nonlocal viscosity, which would lead to the necessary $\partial \eta / \partial \sigma < 0$. A candidate physical process could be particle break-up, since smaller particles lead to a decreased nonlocal viscosity. For instance, if Saturn's ring particles are formed by loosely bound aggregates of smaller solid particles, then increased impact speeds at lower optical depth could lead to an enhanced rate of break-ups in collisions, and thus, to a smaller average particle size. Both effects, smaller particle size and higher dispersion velocity at low optical depth, would work in the right direction, promoting viscous instability.

[3] Simulations of Section 4.3 indicate that at high optical depths gravity wakes can be present also with the Hatzes et al. type elasticity models: however, we have not explored whether such wakes would be consistent with observations. On the other hand, models with dissipative Bridges et al. -type particles match quite well both the A and inner B ring azimuthal brightness asymmetry (Salo et al., 2004; French et al., 2007).

We can demonstrate the principle in terms of a toy model, specifying an ad-hoc decreasing $c(R)$ relation, such that hotter systems have a smaller (average) particle size R. Using this relation, together with the energy balance Eq. (29) and $\tau = \frac{4\sigma}{3R\rho}$, one has three equations to determine τ, R, and σ for given ρ and ε. Here, ρ is the bulk density of the small basic building blocks of the agglomerates. In fact, the density of the agglomerates may be significantly lower. Similarly, the coefficient of restitution ε would represent an effective value for cluster–cluster collisions, which might be considerably lower than ε for the collisions of the small building blocks.

An example is shown in Fig. 19. The assumed $c(R)$ relation is plotted in the upper right panel of the figure, for a range 0.1 m $< R <$ 1m. It uses a parametrization in terms of a tanh-function but a linearly decreasing function would serve the purpose as well. Energy balance leads, together with this relation, to smaller particles for decreasing surface mass density (lower panel, dashed curve), which eventually establishes an only mildly decreasing optical depth (solid curve). The total viscosity arising from this model is shown in the upper panel of the figure. For the chosen parameters (see the figure), a range of surface mass densities between roughly 700 kg/m^2 and 1500 kg/m^2 would be unstable. A ring of surface mass density 1000 kg/m^2, for instance, would develop into ringlets of alternating densities 300 kg/m^2 and 4000 kg/m^2 (roughly). This corresponds to optical depths of one and three, respectively, and particle sizes of decimeters and meters.

If such an effect may lead to a modified form of viscous instability that actually works in Saturn's rings remains to be shown. To this end the physics of cluster formation due to adhesion must be studied, and how it affects the thermal balance of the ring, in order to derive plausible effective cluster sizes depending on the velocity dispersion. For example, if the assumed $c(R)$ relation is significantly colder than the one shown in Fig. 19, or if it is too flat, the region for which $\partial\eta/\partial\sigma < 0$ will shrink, and eventually vanish.

Although following for a self-consistent adjustment of effective particle size on velocity dispersion is beyond the scope of our direct simulations, it is important to check how the viscous instability is modified in the presence of particle size distribution. In principle, it would be possible that the optical depth variations seen in the rings do not represent so much actual surface density differences, but are rather due to variations in the relative concentration of smaller particles against a more or less uniform background of large particles. A possibility of *selective viscous instability* potentially leading to such a concentration of small particles was discussed already in Stewart et al. (1984), who estimated that this would be possible if the small particle have a much larger steady-state velocity dispersion than the large particles: impacts with the large particles could then lead to a reduction of the mean free path of small ones at smaller optical depth than in the case of uni-sized particles. The implied viscosity drop would then make the small particles unstable. However, their analysis neglected nonlocal viscosity, and assumed an elasticity law that would have led to viscous instability also in the identical particle case, just for a slightly larger τ. It is just the nonlocal viscosity that stabilizes, for example, the system following Bridges et al. elasticity law. Also, the assumed velocity ratio, $c_{small}/c_{large} \sim 10^3$ disagrees with numerical simulations (Salo, 1992; Morishima and Salo, 2006; Ohtsuki, 2006). Simulations indicate that size distribution systems stay far from energy equipartition: in practice $c_{small}/c_{large} \leqslant 5$ regardless of the width of the distribution.

Examples of two-particle-size simulations are shown in Fig. 20. The two uppermost rows both display a simulation system that leads to instability in the case of identical particles (Hatzes elasticity model, Bridges type model with increased velocity scale factor $v_c/v_B = 40$; in both cases $\tau = 1$). Instability is also obtained in the case of two particle sizes (here with size ratio $R_2/R_1 = 2$), leading to a clearly stronger contrast among the smaller particles. The lowermost frame displays a case where the identical particle simulation is definitely stable (Bridges type elasticity model with $v_c/v_B = 10$): in a similar two particle case the small particles develop density variations among the more constant background of large ones. However, the amplitude is very small, not really leading to significant contrast between the populations.

Simulations thus suggest that the inclusion of size distribution, although allowing for larger density contrast among the small particles in an otherwise unstable system, does not by itself lead to size-selective instability. However, if we further assume that the particle elasticity depends on particle size, this can lead to selective

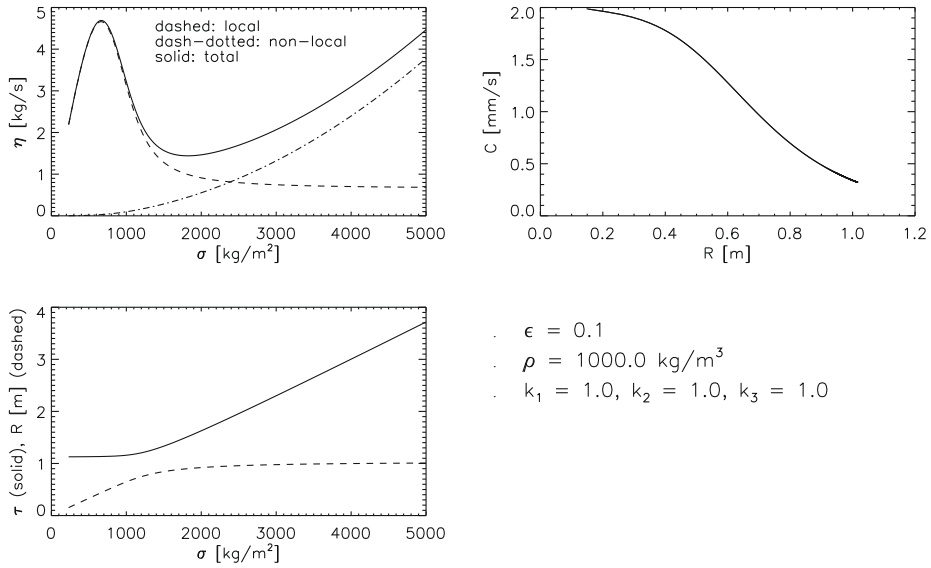

Fig. 19. A toy model for a system where viscous instability is promoted by particle adhesion. Upper right frame: The adopted dependence between velocity dispersion c and effective particle size R, assumed to arise from a balance of coagulation and fragmentation of rubble pile particles. Lower frame: relation between effective particle size (dashed curve) and optical depth (solid curve) on surface density, calculated from the energy balance condition (Eq. (29)) for the assumed $c(R)$ dependence; other used parameter values are indicated in the figure. The reduced particle size and increased velocity dispersion at small surface densities both enhance the local viscosity in comparison to nonlocal viscosity, leading to a $\eta(\sigma)$ relation peaking at intermediate surface densities (upper left frame).

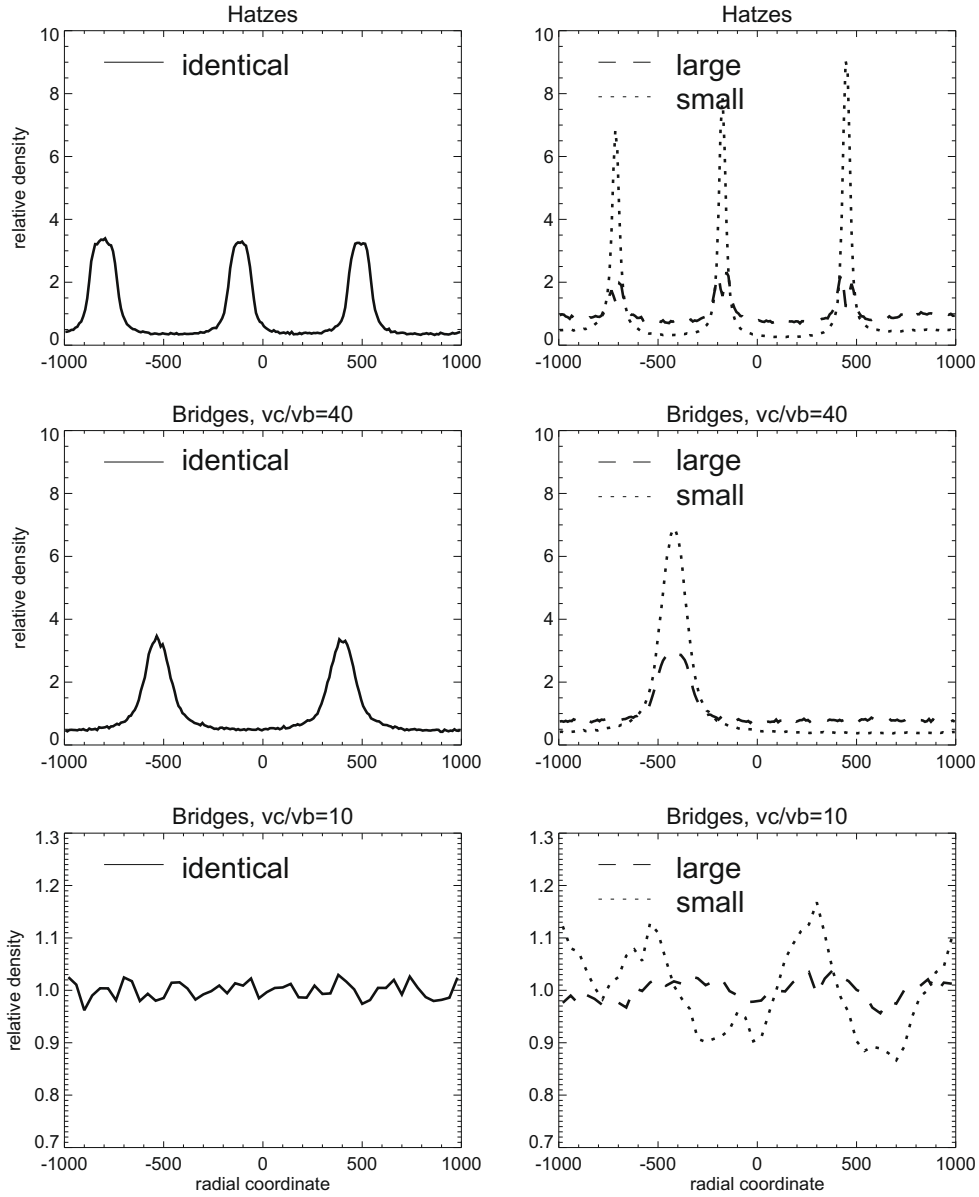

Fig. 20. Viscous instability in two-particle-size systems. The left hand frames show the radial density profiles in simulations of 1 m identical particles with initial optical depth $\tau = 1$, while on the right the system is composed of 1 m and 0.5 m particles, both components having initial optical depths $\tau = 0.5$. The upper row uses Hatzes et al. smooth particle elasticity model (the identical particle case is the same as displayed in Fig. 8 with $N \sim 25,000$ particles; in the two-particle-size case $N \sim 64{,}000$; in all cases the radial and tangential size of the calculation region are 2000 and 40 particle radii), while the next two rows use Bridges et al.-type elasticity laws, either with $v_c/v_B = 40$ (middle row) or $v_c/v_B = 10$ (lowermost row; note the difference in the density scale). The profiles are made from 10 simulation snapshots separated by five orbital periods (corresponds to orbits 955–1000 since the beginning of the simulation).

instability, also in a range of elastic parameters which would otherwise be stable. A preliminary example is provided by Fig. 21. Here two particle sizes with size ratio of $R_2/R_1 = 3$ (mass ratio 27) are used, with $\tau_1 = \tau_2 = 0.5$. The impacts between small particles are more dissipative than those with the large particles: this is at least qualitatively in accordance with what has been found in laboratory experiments of different sized solid ice particles (Dilley and Crawford, 1996). A Bridges et al. type impact law is assumed, except that the parameter v_c is allowed to vary from the original value $v_c = v_B$. We choose $v_c/v_B = 0.1$ for impacts between small particles, making them fairly inelastic, in comparison to impacts between small and large particle where $v_c/v_B = 1$, and in particular in comparison with impacts among large particles for which $v_c/v_B = 10$. After a few hundred orbital periods the system, starting with uniform completely mixed populations, has developed a dense ringlet made predominantly of small particles. The density contrast of small particles is nearly 10, while that for the large ones it is less than two. Note that using $v_c/v_B = 10$ in itself would not lead to instability for any optical depth. Qualitatively, the instability is due to the fact that increasing the partial concentration of small particles at one region reduces their velocity dispersion, since their energy balance becomes dominated by their mutual, very dissipative impacts: this makes the viscosity drop with the relative concentration of small particles. On the other hand, large particles are less affected. Another example is given in Fig. 22: here the scale parameter in the elasticity law for large particles' mutual impacts is reduced from $v_c/v_B = 10$ to $v_c/v_B = 2$. Two ringlets now form in an otherwise similar simulation, with substantially reduced density contrast (less than 3 for small particles and close to unity for the large ones).

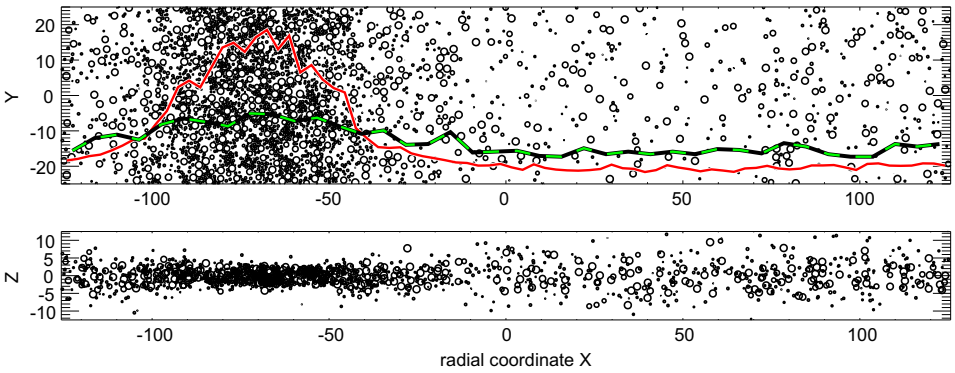

Fig. 21. Example of selective viscous instability. The simulation system consists of two particle sizes, $R = 0.333$ m and $R = 1$ m; both components have $\tau = 0.5$. The size of the calculation region is 250 (radial) and 50 (tangential) m, and the total number of particles is ~20,000. In the initial state both particle sizes are uniformly distributed and here the distribution after 700 orbital periods is displayed. The upper frame shows a slice through the equatorial plane of the system, the lower frame shows a side view, with symbol size corresponding to particle size; only 1/5th of all particles are plotted for clarity. The solid red and black–green dashed curves indicate the density profiles of small and large particles, respectively. In this simulation, v_c/v_B (small–small) = 0.1, v_c/v_B (small–large) = 1.0 and v_c/v_B (large–large) = 10 (see text for explanation) (For interpretation of the references to colour in this figure legend, the reader is referred to the web version of this article.).

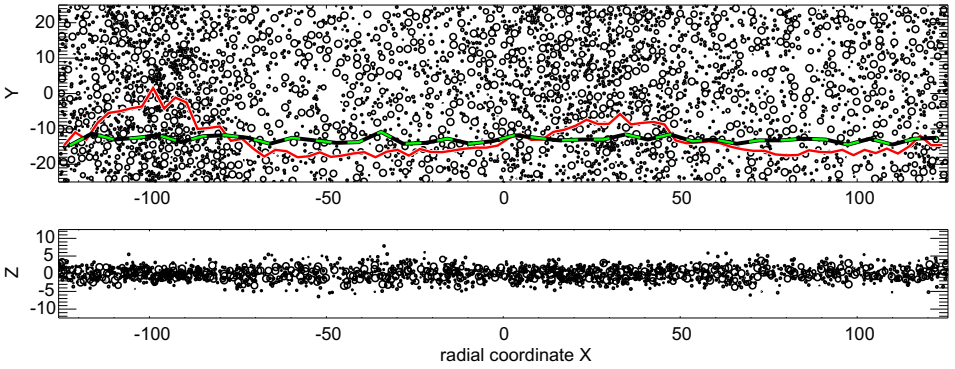

Fig. 22. Like Fig. 21, except that v_c/v_B (small–small) = 0.1, v_c/v_B (small–large) = 1.0 and v_c/v_B (large-large) = 2.

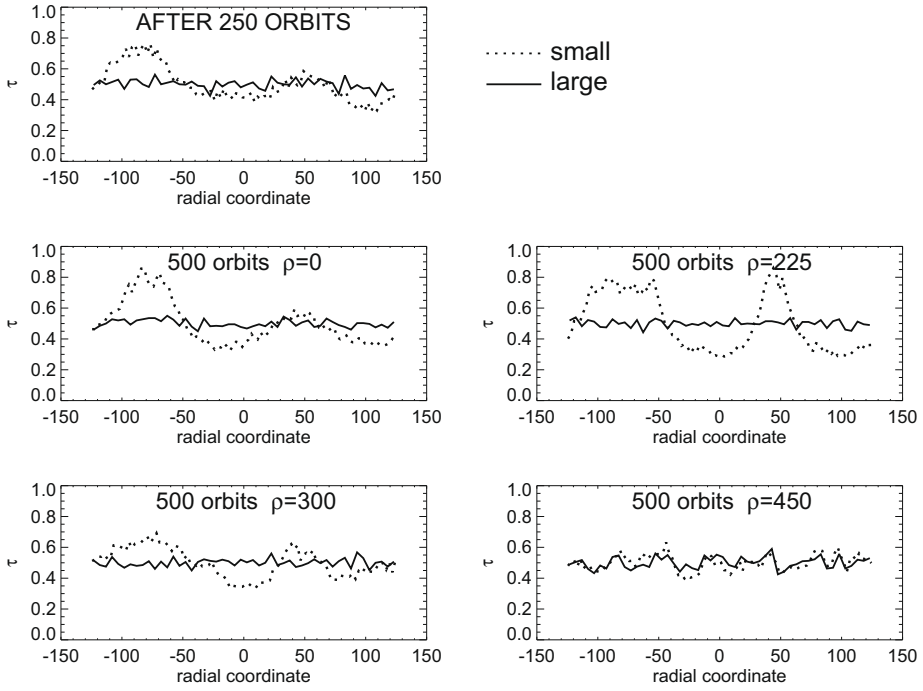

Fig. 23. Effect of self-gravity on selectively unstable two-particle-size systems. The uppermost frame shows a non-gravitating instantaneous impact model simulation which has developed selective viscous instability (the simulation is similar to that in Fig. 22 except that v_c/v_B (large-large) = 3). The next four frames show a continuation of this same run, using the force method code with the inclusion of self-gravity: the internal density of particles is either $\rho = 0$, 225, 300 or 450 kg/m^3. Except for the last case, the concentration of small particles into separate ringlets has been retained, or even somewhat enhanced. In the case with strongest self-gravity the small and large particles become rapidly mixed again: the fluctuations in the profile are due to pronounced gravity wake structure. Note that these runs are preliminary: the tangential width of the simulation region is only 50 m.

We also examined the effect of particle self-gravity on the size dependent selective instability: in principle, gravitational wakes stir the system very efficiently, which might suppress the relative density contrasts among different sized particles. However, simulations (see Fig. 23) indicate that at least in the case of relatively mild self-gravity, the selective instability can be retained, or even slightly enhanced (compare the $\rho = 225\ \mathrm{kg/m^3}$ simulation with $\rho = 0$, the former case showing a stronger concentration of small particles on ringlets). A possible reason is that in the case where global wakes are not formed, the main effect of self-gravity comes via binary encounters. Although gravitational encounters themselves correspond to totally elastic impacts, the mutual acceleration leads to an enhanced dissipation in those encounters which result in a physical impact. As discussed in Salo (1995; see his Fig. 9) the net effect of weak self-gravity can be reduction of the steady state velocity dispersion, which in the current example would further promote the flow of small particles to the ringlets. Nevertheless, with stronger self-gravity (see the $\rho = 450\ \mathrm{kg/m^3}$ case in Fig. 23), the heating by wakes dominates, and all traces of selective instability are removed.

These size-selective instability examples are all preliminary and do not cover the full range of parameters relevant for selective instability. Nevertheless, they highlight an interesting new mechanism which might be relevant for the structure formation in planetary rings.

7. Conclusions

We have demonstrated that viscous instability is possible in direct 3D N-body simulations, using identical particles and a 'smooth particle' elasticity model, based on Hatzes et al. (1988) laboratory experiments. The basic requirement is that the elasticity law is able to maintain a very hot ($\sim \Omega \times 50$ particle radii) velocity dispersion at low optical depths. Comparison to hydrodynamic linear stability analysis verifies the instability condition $\frac{\partial \eta}{\partial \tau} < 0$ (corresponds to $\beta \leqslant -1$, for $\nu \propto \tau^{\beta}$). Also, the simulated linear growth rates agree with the hydrodynamical prediction, but only at the large wavelength limit. The smallest unstable wavelengths are nearly 10 times larger than predicted by the linear isothermal analysis, indicating the importance of thermal effects for the precise instability boundary.

After a relatively rapid growth, an unstable simulation system saturates to a nonlinear quasi steady-state, where dense and rarefied zones co-exist. In this state, a nearly constant value of dynamic viscosity is maintained everywhere in the system. On longer timescales the dense zones gradually merge: 2D experiments indicate that the typical radial separation between ringlets grows proportionally to the square-root of time, as expected for a viscous evolution. Although most of the presented simulation examples led to narrow ringlets separated by lower density regions, the state with narrow lower density 'gaps' among a dense background is also possible, depending on the amount of material on the system (see the 3D $\tau = 1.9$ example in Section 4.2).

The existence of gravity wakes throughout the main A and B rings suggests that the particles in Saturn's rings are rather inelastic, thus not favoring this simplest type of viscous instability. As an attractive possibility, some preliminary examples of size-selective viscous instability are given. This is obtained under the plausible assumption that impacts among small particles are more dissipative than those with large particles. In these 3D simulations the small particles became concentrated to ringlets in a more uniform background of large particles. No extremely high elasticity was required, so that in principle the gravity wake structure can be sustained in such a system. An attractive feature of this selective instability is that the attained density contrast depends on the size ratio and the difference in elastic parameters between the populations: at least in principle this allows for a much richer variety of structures than the simple identical particle model leading to strictly bimodal optical depth variations. Further studies of selective instabilities, including simple analytic modeling are in progress.

Acknowledgments

We acknowledge discussions with Miodrag Sremčević, and thank the reviewers Mark Lewis and Keiji Ohtsuki for their useful suggestions. This work was supported by the Academy of Finland and Deutsches Zentrum für Luft und Raumfahrt (DLR) under Grant 50OH0003.

References

Araki, S., 1991. The dynamics of particle disks III. Dense and spinning particle disks. Icarus 90, 139–171.
Araki, S., Tremaine, S., 1986. The dynamics of dense particle disks. Icarus 65, 83–109.
Bridges, F., Hatzes, A., Lin, D., 1984. Structure, stability and evolution of Saturn's rings. Nature 309, 333–338.
Colwell, J.E., Esposito, L.W., Sremčević, M., 2006. Self-gravity wakes in Saturn's A ring measured by stellar occultations from Cassini. Geophys. Res. Lett. 33, 7201.
Colwell, J.E., Esposito, L.W., Sremcevic, M., Stewart, G.R., McClintock, W.E., 2007. Self-gravity wakes and radial structure of Saturn's B ring. Icarus 190, 127–144.
Daisaka, H., Tanaka, H., Ida, S., 2001. Viscosity in a dense planetary ring with self-gravitating particles. Icarus 154, 296–312.
Dilley, J., Crawford, D., 1996. Mass dependence of energy loss in collisions of icy spheres: An experimental study. J. Geophys. Res. 101, 9267–9270.
French, R.G., Salo, H., McGhee, C.A., Dones, L., 2007. HST observations of azimuthal asymmetry in Saturn's rings. Icarus 189, 493–522.
Goldreich, P., Tremaine, S., 1978. The excitation and evolution of density waves. Astrophys. J. 222, 850–858.
Hämeen-Anttila, K.A., 1978. An improved and generalized theory for the collisional evolution of Keplerian systems. Astrophys. Space Sci. 58, 477–519.
Hämeen-Anttila, K.A., 1982. Saturn's rings and bimodality of Keplerian systems. Moon Planets 26, 171–196.
Hatzes, A., Bridges, F.G., Lin, D.N.C., 1988. Collisional properties of ice spheres at low impact velocities. Mon. Not. R. Astron. Soc. 231, 1091–1115.
Hedman, M.M., Nicholson, P.D., Salo, H., Wallis, B.D., Buratti, B.J., Baines, K.H., Brown, R.H., Clark, R.N., 2007. Self-gravity wake structures in Saturn's A ring revealed by Cassini VIMS. Astron. J. 133, 2624–2629.
Karjalainen, R., Salo, H., 2004. Gravitational accretion of particles in Saturn's rings. Icarus 172, 328–348.
Latter, H.N., Ogilvie, G.I., 2006. The linear stability of dilute particulate rings. Icarus 184, 498–516.
Latter, H.N., Ogilvie, G.I., 2008. Dense planetary rings and the viscous overstability. Icarus 195, 725–751.
Lin, D.N.C., Bodenheimer, P., 1981. On the stability of Saturn's rings. Astrophys. J. Lett. 248, L83–L86.
Longaretti, P.-Y., Rappaport, N., 1995. Viscous overstabilities in dense narrow planetary rings. Icarus 116, 376–396.
Lukkari, J., 1981. Collisional amplification of density fluctuations in Saturn's rings. Nature 292, 433–435.
Morishima, R., Salo, H., 2006. Simulations of dense planetary rings IV. Spinning self-gravitating particles with size distributions. Icarus 181, 272–291.
Ohtsuki, K., 2006. Rotation rate and velocity dispersion of planetary ring particles with size distribution. II. Numerical simulation for gravitating particles. Icarus 183, 384–395.
Papaloizou, J.C.B., Lin, D.N.C., 1988. On the pulsational overstability in narrowly confined viscous rings. Astrophys. J. 331, 838–860.
Salo, H., 1991. Numerical simulations of dense collisional systems. Icarus 92, 367–368.
Salo, H., 1992. Gravitational wakes in Saturn's rings. Nature 359, 619–621.
Salo, H., 1995. Simulations of dense planetary rings. III. Self-gravitating identical particles. Icarus 117, 287–312.
Salo, H., 2001. Numerical simulations of the collisional dynamics of planetary rings. In: Pöschel, T., Luding, S. (Eds.), Granular Gases, Lecture Notes in Physics, vol. 564. Springer Verlag, Berlin, pp. 330–349.
Salo, H., Schmidt, J., Spahn, F., 2001. Viscous overstability in Saturn's B ring: I. Direct simulations and measurement of transport coefficients. Icarus 153, 295–315.
Salo, H., Karjalainen, R., French, R.G., 2004. Photometric modeling of Saturn's rings II. Azimuthal asymmetry in reflected and transmitted light. Icarus 170, 70–90.
Schmidt, J., Salo, H., 2003. A weakly nonlinear model for viscous overstability in Saturn's dense rings. Phys. Rev. Lett. 90 (6), 061102.
Schmidt, J., Salo, H., Spahn, F., Petzschmann, O., 2001. Viscous overstability in Saturn's B ring: II. Hydrodynamic theory and comparison to simulations. Icarus 153, 316–331.
Schmit, U., Tscharnuter, W., 1995. A fluid dynamical treatment of the common action of self-gravitation, collisions, and rotation in Saturn's B-ring. Icarus 115, 304–319.

Shu, F.H., Stewart, G.R., 1985. The collisional dynamics of particulate disks. Icarus 62, 360–383.
Shukhman, I., 1984. Collisional dynamics of particles in Saturn's rings. Sov. Astron. 28, 574–585.
Spahn, F., Schmidt, J., Petzschmann, O., Salo, H., 2000. Stability analyses of a Keplerian disk of granular grains: Influence of thermal diffusion. Icarus 145, 657–660.
Stewart, G.R., Lin, D.N.C., Bodenheimer, P., 1984. Collision-induced transport processes in planetary rings. In: Greenberg, R., Brahic, A. (Eds.), Planetary Rings. Univ. of Arizona Press, Tucson, Arizona, pp. 447–512.
Toomre, A., 1964. On the gravitational stability of a disk of stars. Astrophys. J. 139, 1217–1238.
Toomre, A., Kalnajs, A.J., 1991. Spiral chaos in an orbiting patch. In: Sundelius, B. (Ed.), Dynamics of Disc Galaxies, pp. 341–358.
Ward, W.R., 1981. On the radial structure of Saturn's rings. Geophys. Res. Lett. 8, 641–643.
Wisdom, J., Tremaine, S., 1988. Local simulations of planetary rings. Astron. J. 95, 925–940.